

# A Snapshot of Turbulence in the Northeastern Strait of Magellan

Iossif Lozovatsky<sup>1</sup>, Cristián Escauriaza<sup>2</sup>, Leandro Suarez<sup>3</sup>, Harindra Joseph Fernando<sup>1</sup>, Megan E Williams<sup>4</sup>, Ronald S Coppersmith<sup>1</sup>, and Nicolás Mayorga Mayorga<sup>5</sup>

<sup>1</sup>University of Notre Dame

<sup>2</sup>Pontificia Universidad Católica de Chile

<sup>3</sup>Departamento de Ingeniería Hidráulica y Ambiental. Pontificia Universidad Católica de Chile and <sup>4</sup>Marine Energy Research & Innovation Center (MERIC)

<sup>4</sup>Universidad Técnica Federico Santa María

<sup>5</sup>Departamento de Ingeniería Hidráulica y Ambiental. Pontificia Universidad Católica de Chile

December 10, 2022

## Abstract

First-ever measurements of the turbulent kinetic energy (TKE) dissipation rate in the northeastern Strait of Magellan (Segunda Angostura region) taken in March 2019 are reported here. At the time of microstructure measurements, the magnitude of the reversing tidal current ranged between 0.8 and 1.2 ms<sup>-1</sup>. The probability distribution of the TKE dissipation rate in the water interior above the bottom boundary layer was lognormal with a high median value  $\epsilon_{med} = 1.2 \times 10^{-6}$  Wkg<sup>-1</sup>. Strong vertical shear,  $(1-2) \times 10^{-2}$  s<sup>-1</sup> in the weakly stratified water interior ensued a sub-critical gradient Richardson number,  $Ri < 10^{-1} - 10^{-2}$ . In the bottom boundary layer (BBL), the vertical shear and the TKE dissipation rate both decreased exponentially with the distance from the seafloor  $\zeta$ , leading to a turbulent regime with the eddy viscosity  $K \sim 10^{-3}$  m<sup>2</sup>/s, which varied with the time and location, while being independent of the vertical coordinate in the upper part of BBL (for  $\zeta > \sim 2$  meters above the bottom).

# A Snapshot of Turbulence in the Northeastern Strait of Magellan

I. D. Lozovatsky<sup>1</sup>, C. Escauriaza<sup>3</sup>, L. Suarez<sup>3,4</sup>, H. J. S. Fernando<sup>1,2</sup>, M. E. Williams<sup>5</sup>, R. S. Coppersmith<sup>1</sup>, and N. Mayorga<sup>3</sup>

<sup>1</sup>Department of Civil & Environmental Engineering & Earth Sciences, University of Notre Dame, USA

<sup>2</sup>Department of Aerospace and Mechanical Engineering, University of Notre Dame, USA

<sup>3</sup>Departamento de Ingeniería Hidráulica y Ambiental. Pontificia Universidad Católica de Chile, Chile

<sup>4</sup>Marine Energy Research & Innovation Center (MERIC), Santiago, Chile.

<sup>5</sup>Departamento de Obras Civiles. Universidad Técnica Federico Santa María, Valparaíso, Chile

Corresponding author Iossif Lozovatsky ([i.lozovatsky@nd.edu](mailto:i.lozovatsky@nd.edu))

## Key Points:

- Results of first ever direct measurements of small-scale turbulence in the Strait of Magellan conducted using a microstructure profiler VMP-500 are reported.
- Above the bottom boundary layer, the probability distribution of turbulent kinetic energy (TKE) dissipation rate was lognormal with a median exceeding  $10^{-6} \text{ Wkg}^{-1}$ .
- In the BBL, the mean shear and TKE dissipation rate decreased exponentially with the distance from the seafloor  $\zeta$  leading to an eddy viscosity  $\sim 10^{-3} \text{ m}^2\text{s}^{-1}$  independent on  $\zeta$ .

## 29 **Abstract**

30 First-ever measurements of the turbulent kinetic energy (TKE) dissipation rate in the  
31 northeastern Strait of Magellan (Segunda Angostura region) taken in March 2019 are reported  
32 here. At the time of microstructure measurements, the magnitude of the reversing tidal current  
33 ranged between 0.8 and 1.2 ms<sup>-1</sup>. The probability distribution of the TKE dissipation rate in the  
34 water interior above the bottom boundary layer was lognormal with a high median value  
35  $\varepsilon_{med}^{MS} = 1.2 \times 10^{-6}$  Wkg<sup>-1</sup>. Strong vertical shear,  $(1-2) \times 10^{-2}$  s<sup>-1</sup> in the weakly stratified water  
36 interior ensued a sub-critical gradient Richardson number,  $Ri < 10^{-1} - 10^{-2}$ . In the bottom  
37 boundary layer (BBL), the vertical shear and the TKE dissipation rate both decreased  
38 exponentially with the distance from the seafloor  $\zeta$ , leading to a turbulent regime with the eddy  
39 viscosity  $K_M \sim 10^{-3}$  m<sup>2</sup>/s, which varied with the time and location, while being independent of  
40 the vertical coordinate in the upper part of BBL (for  $\zeta > \sim 2$  meters above the bottom).

## 41 **Plain Language Summary**

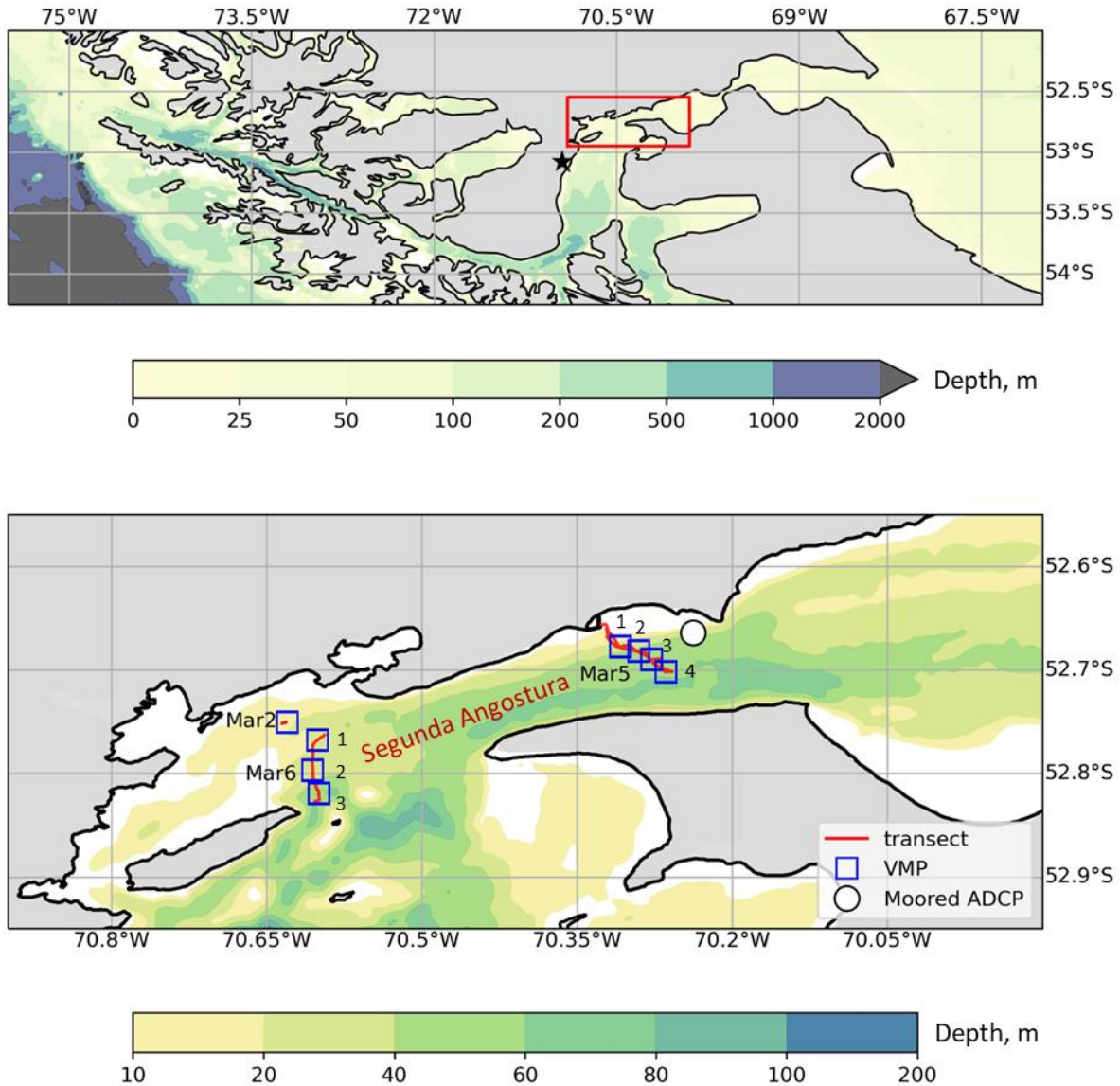
42 The Strait of Magellan (MS) is a narrow  $\sim 2$  km wide and  $\sim 500$  km long waterway that  
43 meanders between the Atlantic and Pacific oceans, separating Patagonia from Tierra del Fuego.  
44 The Strait is an environmentally unique, and undergoes rapid ecological changes due to  
45 anthropogenic stressors. To study small-scale marine turbulence in the region, which influences  
46 vertical transport of heat, momentum, nutrients, sediments and other substances, we conducted  
47 first ever direct measurements of turbulent kinetic energy (TKE) dissipation rate  $\varepsilon$  in the  
48 northeastern part of the Strait (Segunda Angostura narrow) using a vertical microstructure  
49 profiler. The most notable finding is the very high level of turbulence existing near the seafloor,  
50 signified by  $\varepsilon_b \approx 10^{-3}$  Wkg<sup>-1</sup>, which is among the highest TKE dissipation rate measured  
51 previously by numerous authors in various narrow tidal channels. Tidal currents in MS generated  
52 a turbulent bottom boundary layer (BBL) with an exponential decay of the dissipation rate and  
53 the mean velocity gradient (vertical shear) toward the water interior. This turbulent regime can  
54 be specified by the eddy viscosity on the order of  $\sim 10^{-3}$  m<sup>2</sup>/s that varied with time and location  
55 while being independent of the vertical coordinate  $\zeta$  in the upper part of BBL (for  $\zeta > \sim 2$   
56 meters above the bottom). The measurements described has only limited information on the  
57 specifics of turbulence in MS, calling for further investigations of turbulence and mixing therein.

## 58 **1 Introduction**

59           The Strait of Magellan (henceforth also the Magellan Strait (MS) or just the Strait) is an  
60 environmentally unique region being, in particular, a feeding ground to humpback whales  
61 (Acevedo et al., 2011). The region currently experiences changes of its ecological balance due to  
62 anthropogenic stressors such as excessive fishing, offshore oil production and newly leased areas  
63 for aquaculture. Understanding of small-scale dynamical processes in the Magellan Strait is  
64 paramount for multidisciplinary studies of physical, biogeochemical and ecological processes in  
65 the coastal regions of Patagonia. For this reason, we launched the first ever in-situ measurements  
66 of the kinetic energy dissipation rate in the north-eastern part of the Strait to obtain estimates of  
67 turbulence and mixing across the water column down to the bottom boundary layer (BBL).

68           The Strait of Magellan is a narrow  $\sim 1.1$  nautical miles (NM) waterway that meanders  
69 between the Atlantic and Pacific oceans, separating Patagonia from Tierra del Fuego; it is about  
70 310 NM long (Figure 1). According to Simeoni et al. (1997), the mean annual air temperature of  
71 the eastern MS is  $6 - 7^\circ \text{C}$ , varying from  $8^\circ$  to  $11^\circ \text{C}$  in the summer (December - February) and  
72 from  $2^\circ$  to  $3^\circ \text{C}$  in the winter (June-August). Easterly-directed winds of characteristic speed  $7$   
73  $\text{ms}^{-1}$  are typical in the region (Garreaud et al., 2013). Stormy winds (up to  $25 \text{ms}^{-1}$ ) are often  
74 observed during winter and spring seasons.

75           Strong barotropic tidal flow and winds are the major drivers of mesoscale circulation in  
76 the Strait. On the Atlantic side, the Strait is characterized by high-amplitude semidiurnal tides  
77 with a mean tide range of  $7.1 \text{m}$ , which gradually decreases to about  $1.5 - 2 \text{m}$  toward Punta  
78 Arenas (see Figure 4 of Medeiros & Kjerfve, 1988). Tidal amplification occurs in a series of  
79 narrows at the Atlantic side to the northeast of Punta Arenas (Figure 1), for example, in Segunda  
80 Angostura (SA), where our pilot field campaign was conducted (see also detailed map of SA in  
81 Figure 1 of Lutz et al., 2016). The seabed in SA is mainly composed of hard substratum and  
82 outcropping rocks (Simeoni et al., 1997). High level of tidally induced turbulence is an expected  
83 phenomenon in SA as has been reported in several recent publications on turbulence in narrow  
84 tidal channels elsewhere (e.g., McMillan et al., 2016; Horwitz & Hay, 2017; Guerra & Thomson,  
85 2017; Ross et al., 2019).



86

87 **Figure 1.** Upper panel: the measurement site (bounded by a red box) in the main passage of the Magellan  
 88 Strait to the NNE from Punta Arenas (black star). Lower panel: an enlarged section of the Magellan Strait  
 89 showing locations of the VMP stations (squares marked by the date and station numbers); the ADCP  
 90 mooring (a white circle). Two separate color palettes (scales) specify the mean water depth of the upper  
 91 and lower panels, respectively. Segunda Angostura is a narrower channel in the Atlantic sector of the  
 92 Magellan Strait.

93 Very limited information exists on hydrological characteristics of the Magellan waters.  
 94 Antezana (1999) reported basic hydrographic features (temperature and salinity) in the main  
 95 passages of the Strait and suggested that adjacent oceanic waters were warmest in the Atlantic  
 96 and saltiest in the Pacific sectors, maintaining an along-strait horizontal T-S gradient.  
 97 Precipitations and continental freshwater discharge to the Strait induce patterns of the diluted

98 near surface waters transported to the Atlantic Patagonian shelf (Brun et al., 2020). The large-  
99 scale hydrological features as well as seasonal variations of mesoscale circulation may influence  
100 turbulence in the Strait, but strong tides and local winds are the most likely generators of  
101 turbulence in the shallow Atlantic sector of the MS.

102 To shed light on characteristics of small-scale turbulence in MS, a short field campaign  
103 was carried out in the northeastern part of the Strait using a vertical microstructure profiler  
104 VMP-500 and acoustic Doppler current profilers (section 2). Patterns of tidal currents during the  
105 microstructure measurements are described in section 3.1. Sections 3.2 and 3.3 present several  
106 examples of the TKE dissipation rate profiles comparing the level of turbulence in well-mixed  
107 water interior of MS (section 3.3) with turbulence intensity (illustrated by log-normal  
108 distribution functions of the dissipation rate) of homogeneous non-stratified layers in other  
109 kindred oceanic regions. Specifics of turbulence and mean current shear profiles in the BBL of  
110 Segunda Angostura are discussed in section 3.4 vis-à-vis our own measurements carried out in  
111 various tidally affected shallow seas. The main results are summarized in section 4, including a  
112 comparison of turbulence measurements in narrow tidal channels elsewhere.

## 113 **2 Measurements**

114 Turbulence and stratification in the Strait were measured using a Vertical Microstructure  
115 Profiler, VMP-500, (<http://rocklandscientific.com/products/profilers/vmp-500/>). Airfoil probes  
116 were used to estimate small-scale shear, enabling the calculation of TKE dissipation rate  $\varepsilon(z)$ ,  $z$   
117 being the (downward) vertical coordinate. An accelerometer, pressure sensor and a SeaBird  
118 temperature-conductivity package provided precise salinity, temperature and potential density  
119 profiles. The airfoil sensors were calibrated by Rockland Scientific prior to and after the field  
120 campaign. The measurements were taken from a medium-size fishing boat, Marypaz II. The ship  
121 was equipped with A-frame at the rear deck, which was used to recover the VMP after each cast  
122 conducted in a free-falling mode with a thin tethered cable of neutral buoyancy. We were able to  
123 keep the VMP sinking velocity constant,  $W \sim 0.7 \text{ ms}^{-1}$  (see Appendix), with a sharp drop off to  
124 zero at the end of the casts (usually at  $\sim 1\text{-}2$  m above the bottom)

125 A shipboard acoustic Doppler current profiler (ADCP) measured vertical profiles of  
126 zonal  $u(z)$  or  $u(\zeta)$  and meridional  $v(z)$  or  $v(\zeta)$  velocity components. Here, the distance

127 from the sea surface  $z$ ,  $\zeta = z_b - z$  is a distance from the sea floor in meters above the bottom  
128 (mab) and  $z_b$  is the bottom depth in point at the time of measurements. A Teledyne Workhorse  
129 sentinel ADCP operated at 600 kHz with high vertical resolution (1-m bin size), but the  
130 measurements were restricted to the depth range  $z = 1 - 49$  m. Processing of the VMP and ADCP  
131 data followed well-established methodology adopted during our previous field campaigns (e.g.,  
132 Lozovatsky et al., 2019, 2021; see also Roget et al., 2006 and Goodman et al., 2006). Multiple  
133 GPS systems were on board, but an automatic weather station was not present; thus, the  
134 meteorological conditions at Punta Arenas during the cruise were used as local.

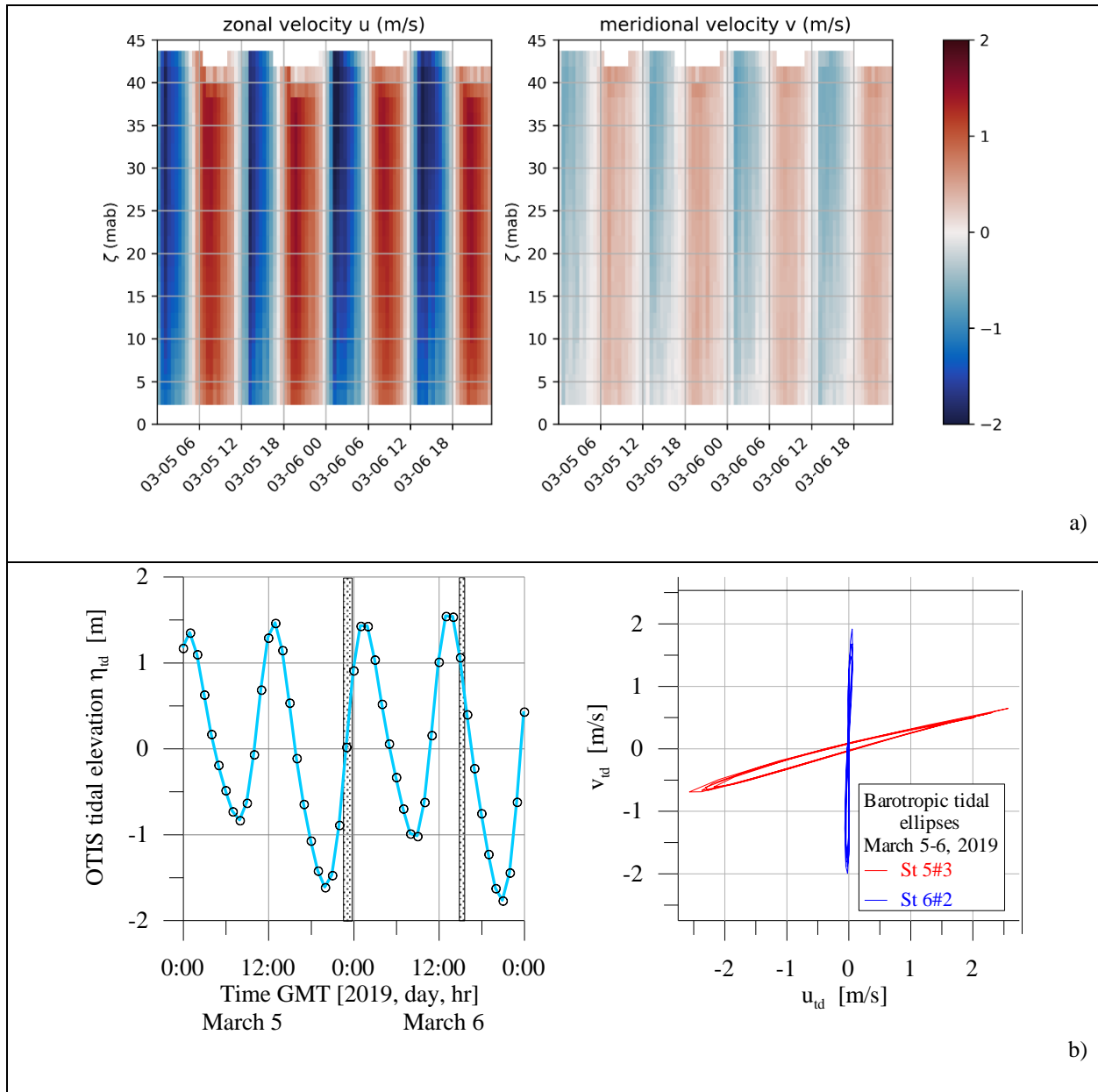
135 The VMP-500 was successfully deployed at eight stations near the eastern and western  
136 ends of Segunda Angostura (SA) of the Magellan Strait (Figure 1). The first test station was  
137 taken on March 2 near the coast (the bottom depth  $z_b \sim 21$  m) under calm weather conditions  
138 (wind speed 2-3  $\text{ms}^{-1}$ ). This appears to be the only VMP station wherein a weak but  
139 distinguishable temperature, salinity and density stratifications of the water column were  
140 observed. On March 3, a bottom-mounted ADCP mooring was setup in the northern part of SA  
141 (see Figure 1), but the VMP measurements on March 3 and 4 were suspended due to rough seas  
142 (wave height up to 2 m) and high winds that periodically exceeded 10-12  $\text{ms}^{-1}$ . Toward the end  
143 of the day of March 5 the stormy wind ceased, permitting to conduct four VMP stations in the  
144 central part of SA (closer to its eastern entrance,  $\varphi = 52^\circ 39'58'' - 52^\circ 42'7''$  S,  $\lambda = 70^\circ 19'0'' -$   
145  $70^\circ 15'51''$  W; with  $z_b$  varying from 30 to 57 m). The measurements continued on March 6 at  
146 three stations across the Strait about four miles to the west off the western SA entrance ( $\varphi =$   
147  $52^\circ 53'54'' - 52^\circ 49'5''$  S,  $\lambda = 70^\circ 49'59'' - 70^\circ 38'58''$  W with  $z_b$  varying from 26 to 57 m).  
148 Positions of all VMP stations are shown in Figure 1.

### 149 **3 Results**

#### 150 **3.1 Tidal flow**

151 Basic tidal characteristics in the SA area of MS are given in Figure 2 for two main days of  
152 VMP measurements (March 5-6, 2019). The ADCP current components  $u(\zeta, t)$  and  $v(\zeta, t)$  at  
153 the mooring location are shown in Figure 2a and the tidal elevation  $\eta_{td}(t)$  and tidal ellipses are  
154 in Figure 2b. It appears that a semidiurnal tide ( $\omega_{td} = 1.41 \times 10^{-4} \text{ s}^{-1}$ ) with current amplitude  $\sim 2$

155  $\text{ms}^{-1}$  and surface elevation  $\sim 1.5$  m was a dominant background force governing mean currents  
 156 that generated small-scale turbulence in the SA region. The tidal ellipses (Figure 2b) are highly  
 157 stretched in NE-SW direction along the SA axis in the middle of the narrow channel.



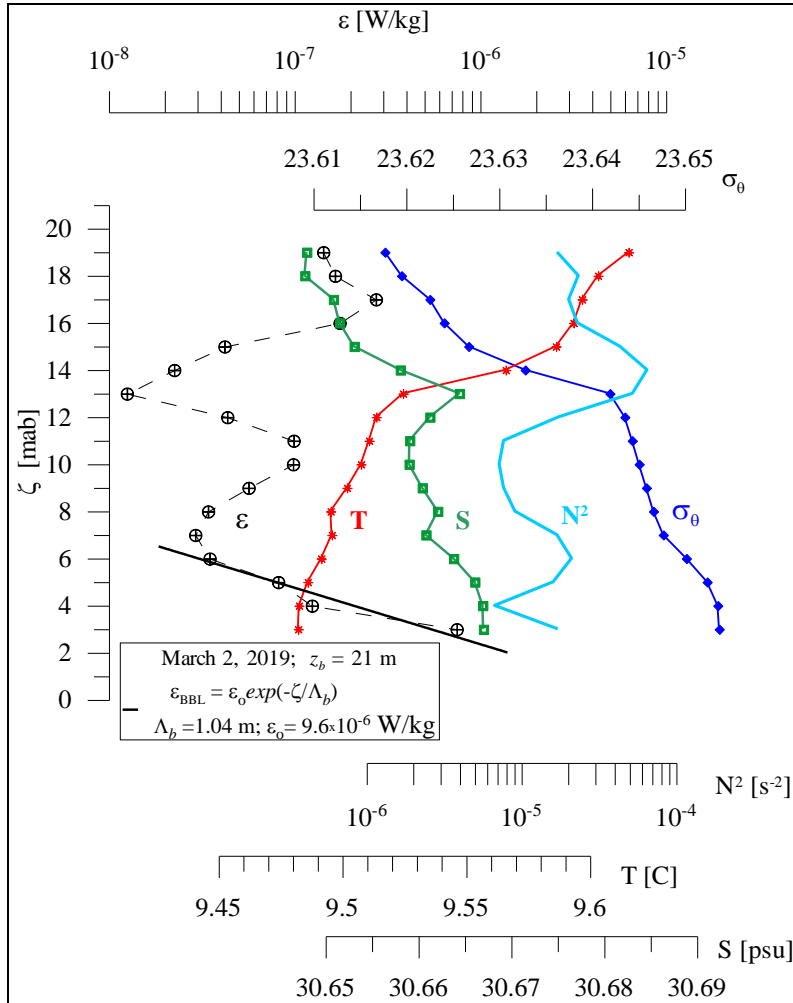
158 **Figure 2.** a) - ADCP current components at the mooring location (see Figure 1) for March 5-6, 2019  
 159 (color scale in  $\text{ms}^{-1}$ ; b) left - tidal elevation in SA based on modeling data of OTIS (OSU Tidal Inversion  
 160 Software, courtesy of S. Erofeeva; <https://www.tpxo.net/otis>). Periods of VMP measurements are marked  
 161 by grey segments; b) right – OTIS barotropic tidal ellipses in SA for St.5#3 and St. 6#2.

162 To the west of SA, the dominant tidal current was in the S-N direction with a large  
 163 amplitude meridional component ( $v_{tid} \approx \pm 2 \text{ ms}^{-1}$ ) and a very small zonal component ( $u_{tid} \approx \pm 0.07$

164  $\text{ms}^{-1}$ ). Note that the VMP measurements were taken during rising tide on March 5 and during  
 165 subsiding tide on March 6, both not at the periods of maximum tidal velocities due to the  
 166 operational constrains.

### 167 3.2 MS turbulence: stable ambient stratification

168 Figure 3 shows the TKE dissipation rate profile  $\varepsilon(\zeta)$  obtained on March 2 at the  
 169 beginning of field campaign under light winds ( $2\text{-}3 \text{ ms}^{-1}$ ).



170

171 **Figure 3.** Profiles of the TKE dissipation rate  $\varepsilon(\zeta)$ , temperature  $T(\zeta)$ , salinity  $S(\zeta)$ , potential  
 172 density  $\sigma_\theta(\zeta)$ , and squared buoyancy frequency  $N^2(\zeta)$  observed under light winds to the west from  
 173 SA. Here  $\zeta$  is the distance above the bottom in meters (mab).

174 The background density stratification was characterized by  $N^2 \sim 2 \times 10^{-5} \text{ s}^{-2}$  for the upper  
 175 weakly stratified 5 meters of the water column ( $\zeta > 16$  mab), increasing to  $\sim 6 \times 10^{-5} \text{ s}^{-2}$  in a

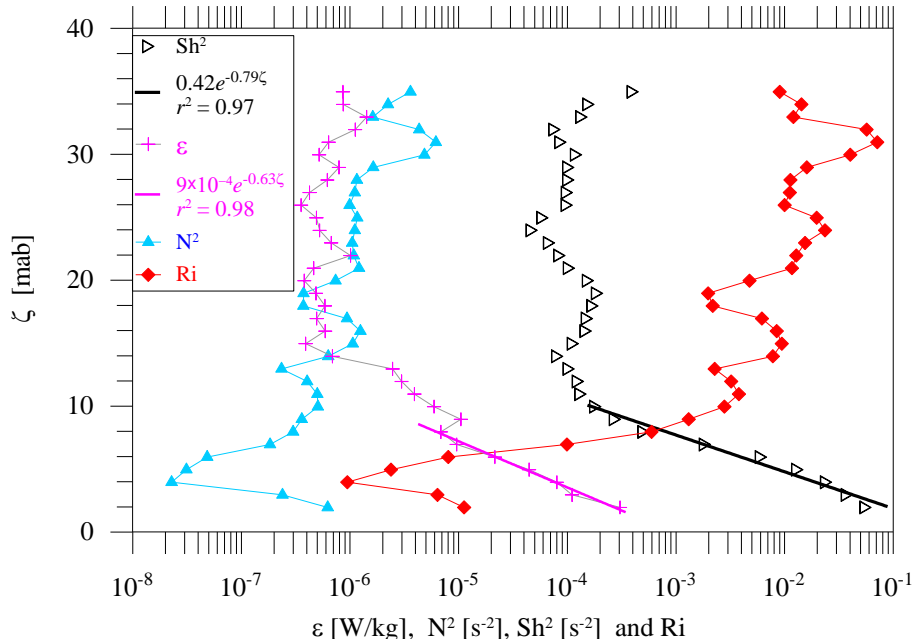
176 narrow,  $\zeta = 13 - 16$  mab, pycnocline (thermocline). Then it generally decreased to  
 177  $N^2 \sim (0.9 - 2) \times 10^{-5} \text{ s}^{-2}$  below the pycnocline ( $\zeta < 11 - 12$  mab). The TKE dissipation rate profile  
 178 shows relatively high  $\varepsilon \approx (1 - 2) \times 10^{-7} \text{ Wkg}^{-1}$  in the near surface layer, decreasing to  $\varepsilon \sim 10^{-8}$   
 179  $\text{Wkg}^{-1}$  in the pycnocline. Starting from  $\zeta \sim 6$  mab, however,  $\varepsilon(\zeta)$  clearly exhibited an  
 180 exponential growth toward the seafloor (black line in Figure 3), reaching  $\varepsilon \sim 8 \times 10^{-7} \text{ Wkg}^{-1}$  at  $\zeta$   
 181  $\sim 3$  mab. Note that at this shallow station the VMP did not descend closer to the bottom, where  $\varepsilon$   
 182 could perhaps rise by another order of magnitude. The TKE dissipation in the interior of stratified  
 183 water column,  $\varepsilon \sim (1 - 3) \times 10^{-8} \text{ Wkg}^{-1}$ , appears to be comparable with (but at the higher end of)  
 184 the dissipation estimates obtained in our previous measurements on shallow stratified *tidal* shelves  
 185 elsewhere (see  $\varepsilon(\zeta)$  profiles presented later in Figure 6). Note that even in narrow tidal channels  
 186 (e.g., Sansum Narrows, which separates Vancouver and Saltspring Islands in British Columbia,  
 187 Canada; flooding tide of  $\sim 2 \text{ ms}^{-1}$ ) turbulence is strongly affected by layers of stable stratification,  
 188 dropping  $\varepsilon < 10^{-8} \text{ Wkg}^{-1}$  (Wolk & Lueck, 2012).

### 189 **3.3 MS turbulence: well-mixed water interior**

190 After stormy winds ( $10-12 \text{ ms}^{-1}$ ) on March 4, the water column in SA was almost  
 191 completely mixed, being characterized by very low buoyancy frequency  $N^2$  in the range  
 192  $2 \times (10^{-7} - 10^{-6}) \text{ s}^{-2}$ . Figure 4 shows vertical profiles of  $N^2(\zeta)$ ,  $Sh^2(\zeta)$  (the squared vertical  
 193 shear, ship-based ADCP measurements), the gradient Richardson number  
 194  $Ri(\zeta) = N^2(\zeta)/Sh^2(\zeta)$  and  $\varepsilon(\zeta)$  to demonstrate properties of well-mixed tidal flow in the  
 195 MS. Vertical structure of all variables in Figure 4 consists of two distinct layers. The first is the  
 196 bottom boundary layer, where the dissipation rate exponentially increases with depth (  
 197  $\zeta < \zeta_{BBL} \approx 8$  mab) mirroring an exponential increase of vertical shear and corresponding  
 198 decrease of  $Ri(\zeta)$ . Although  $N^2(\zeta)$  shows slight increase in two meters just above the  
 199 seafloor, the values of  $N^2 < 7 \times 10^{-7} \text{ s}^{-2}$  are still extremely low.

200 Another major layer covers the water column above the BBL ( $\zeta > \zeta_{BBL}$ ), where the shear  
 201 and the dissipation rate vary around the means  $\langle \varepsilon \rangle = 6.8 \times 10^{-7} \text{ Wkg}^{-1}$  and  $\langle Sh^2 \rangle = 1.1 \times 10^{-4} \text{ s}^{-2}$

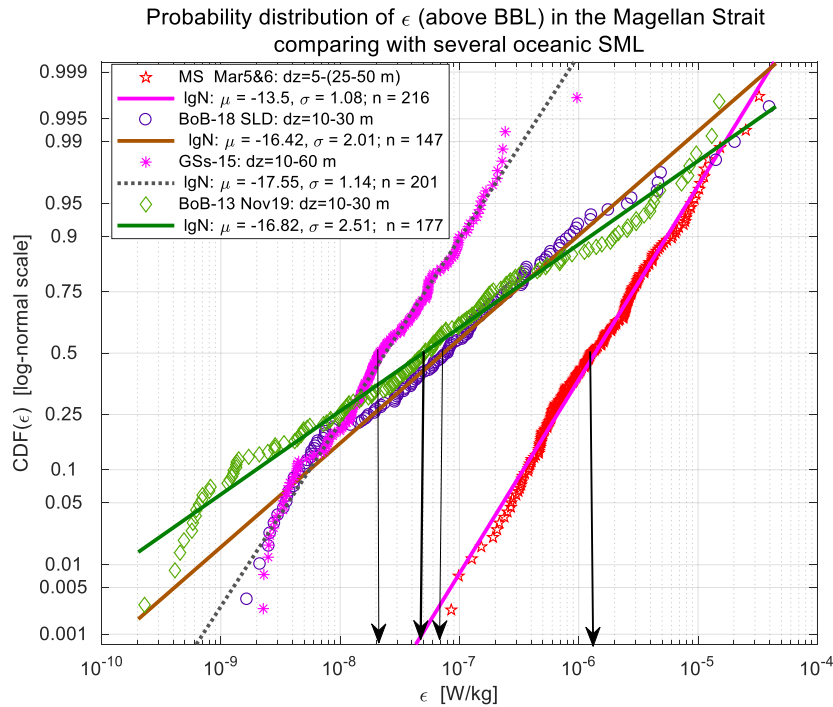
202 for an example in Figure 4. Statistical behavior of such random variable as  $\varepsilon$  can be specified in  
 203 terms of the cumulative probability distribution function  $CDF(\varepsilon)$ , which is shown in Figure 5  
 204 by red pentagrams, calculated using all dissipation samples pertained to the depth range between  
 205  $z_o = 5$  m and  $z_{BBL} = 25 - 50$  m depending on the BBL height  $\zeta_{BBL}$  in every specific VMP cast.  
 206



207  
 208 **Figure 4.** An example of the vertical profiles of squared buoyancy frequency  $N^2(\zeta)$ , mean shear  
 209  $Sh^2(\zeta)$ , gradient Richardson number  $Ri(\zeta)$ , and dissipation rate  $\varepsilon(\zeta)$  obtained on March 6 in the  
 210 mixed waters of MS (signified by very small values of  $N^2(\zeta)$  in the entire water column). Station 6#2  
 211 in Figure 1.

212 To compare turbulence intensity in homogeneous waters of MS with non-stratified  
 213 turbulence in oceanic regions elsewhere, Figure 5 shows several examples of  $CDF(\varepsilon)$  obtained  
 214 for surface mixed layers (SML) in the northern (Jinadasa et al., 2016) and southwestern  
 215 (Lozovatsky et al., 2019) Bay of Bengal (BoB-13 and BoB-18, respectively) and in the Gulf  
 216 Stream region (GS-15). Those  $CDF(\varepsilon)$  were calculated for  $z = 10$  to 30 m for relatively shallow  
 217 SML underlain by a sharp pycnocline in both BoB regions (moderate local winds) and  $z = 10$  to  
 218 50 m in a deep, well-developed SML for GS-15 (Lozovatsky et al., 2017a).

219 As expected, all  $CDFs(\epsilon)$  in Figure 5 are well approximated by lognormal probability  
 220 distribution of the Gurvich & Yaglom (1967) model as well as numerous data obtained in non-  
 221 stratified marine layers (e.g., Lozovatsky et al., 2017b; McMillan & Hay, 2017). Furthermore,  
 222 Figure 5 indicates that turbulence in SA is much stronger than that typically observed in oceanic  
 223 SML under similar (low and moderate) winds. The median value of the TKE dissipation rate in  
 224 the MS above the BBL  $\epsilon_{med}^{MS} = 1.2 \times 10^{-6} \text{ Wkg}^{-1}$  is an order of magnitude higher than that in the  
 225 SML  $CDFs$  shown in Figure 5, where  $\epsilon_{med}^{SML} \approx (2-7) \times 10^{-7} \text{ Wkg}^{-1}$ . Such high level of turbulence  
 226 appears to be governed by shear instability developed across the entire water column in the SA  
 227 region, where  $\langle Sh^2 \rangle = 1.1 \times 10^{-4} \text{ s}^{-2}$  and highly subcritical  $Ri$  values, varying above the BBL  
 228 mostly in the range  $Ri \sim 0.01 - 0.1$ .



229

230 **Figure 5.** Cumulative distribution functions of the dissipation rate  $CDF(\epsilon)$  for mixed water interior of  
 231 the Magellan Strait (MS 2019, March 5&6 data) and examples of  $CDF(\epsilon)$  for oceanic surface mixed  
 232 layer (SML) under light and moderate winds. Those measurements were taken in the northern and  
 233 southern Bay of Bengal (BoB-13 and BoB-18, respectively) and in the Gulf Stream (GS-15). The depth  
 234 ranges selected for  $CDF(\epsilon)$  calculation, the number of CDF samples  $n$  and parameters of lognormal  
 235 approximations of the empirical distributions  $\mu$  and  $\sigma$  are in the legend. The arrows point to the  
 236 corresponding median values.

237 **3.4 MS turbulence: BBL**

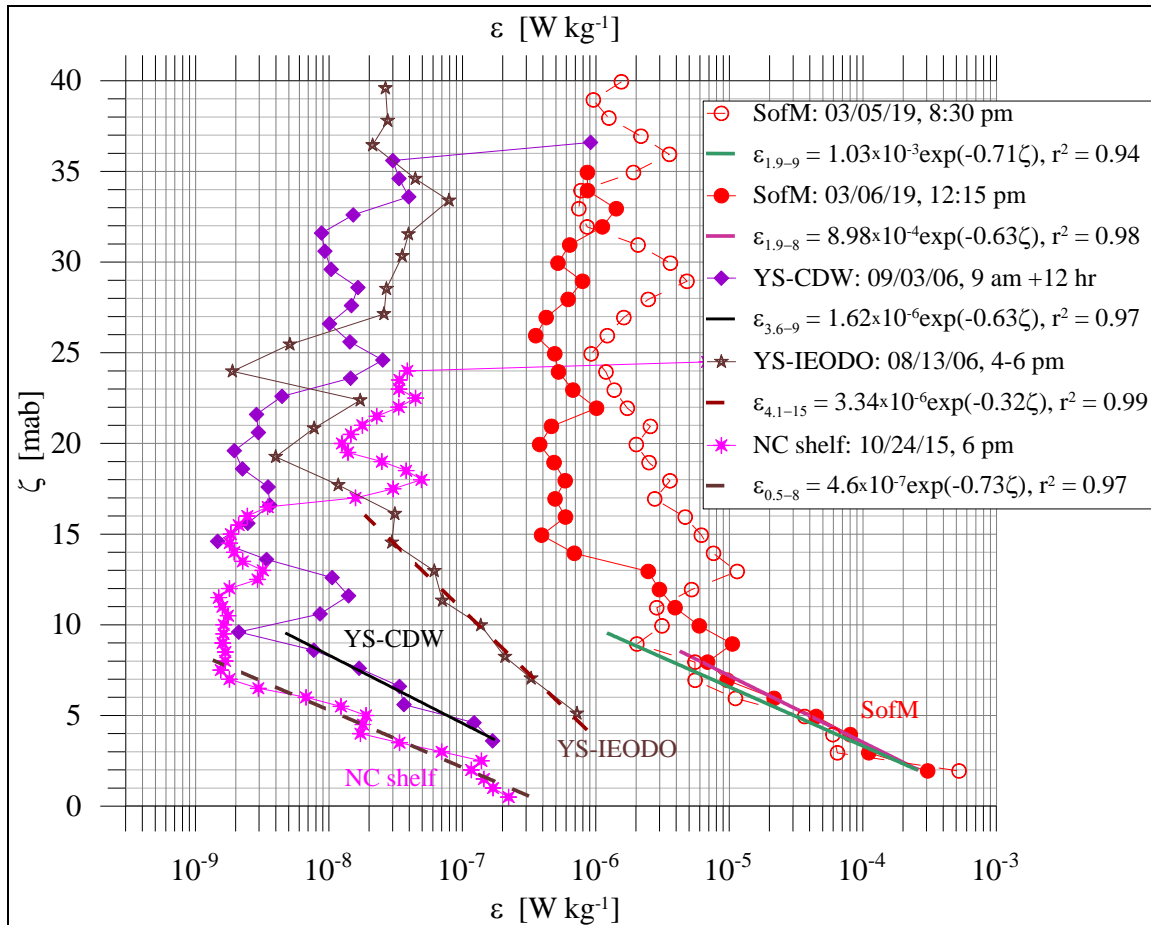
238 The BBL in well-mixed waters of MS was not distinct in thermohaline profiles due to  
239 very small differences in temperature, salinity, and density near the bottom, but the BBL was  
240 easy to define in the profiles of the squared mean shear  $Sh^2(\zeta)$  and the dissipation rate  $\varepsilon(\zeta)$ .  
241 The TKE dissipation profiles  $\varepsilon(\zeta)$  shown in Figures 3 and 4 clearly indicate that starting from  
242 some distance above the bottom  $\zeta_{BBL} = z_b - z_{BBL}$ , the dissipation rate sharply (exponentially)  
243 increases toward the seafloor. All  $\varepsilon(\zeta)$  profiles in the MS showed an exponential dependence  
244  $\varepsilon$  on  $\zeta$

245 
$$\varepsilon(\zeta) = \varepsilon_b e^{-\zeta/\Lambda} \quad (1)$$

246 where  $\varepsilon_b$  is the dissipation rate near the bottom and  $\Lambda$  a characteristic external length scale for  
247 shear generated turbulence by mean (tidal) flow. Two additional  $\varepsilon(\zeta)$  profiles typical of March  
248 5 and 6 are given in Figure 6 along with several profiles of  $\varepsilon(\zeta)$  obtained elsewhere in shallow  
249 tidal seas, where an exponential decrease of  $\varepsilon$  with  $\zeta$  in BBL is demonstrated. These latter  
250 data were collected in the Changjiang River Diluted Waters (YS-CDW) in the southwestern  
251 Yellow Sea (Lozovatsky et al., 2012), in the IEODO region (YS-IEODO) in the southeastern  
252 Yellow Sea (Lozovatsky et al., 2015) as well as on the North Carolina (NC) shelf (Lozovatsky et  
253 al., 2017a). Note that an exponential decay of  $\varepsilon(\zeta)$  has been suggested by St. Laurent et al.  
254 (2002) for deep-ocean BBL as a possible model of  $\varepsilon(\zeta)$  for turbulence generated by internal  
255 tidal energy flux propagated upward over rough abyssal bathymetry.

256 All dissipation rate profiles in shallow BBL shown in Figure 6 can be well-approximated  
257 by formulae (1) with coefficient of determination  $r^2 = 0.94 - 0.99$ . The tallest turbulent BBL with  
258 exponentially varying  $\varepsilon(\zeta)$  was observed in the YS-IEODO region ( $\zeta_{BBL} \sim 15$  mab,  $\Lambda = 3.1$  m)  
259 while a characteristic height of such BBL in other regions was  $\zeta_{BBL} \sim 8 - 9$  mab with  
260  $\Lambda = 1.4 - 1.6$  m. It is worth noting that for all  $\varepsilon(\zeta)$  profiles in Figure 6, the external turbulent  
261 scale  $\Lambda \sim 0.2\zeta_{BBL}$ , which is a typical value for boundary-induced turbulence (e.g., Monin &

262 Yaglom 1971). An exponential decrease of  $\varepsilon(\zeta)$  within the YS-IEODO BBL has been observed  
 263 by Lozovatsky et al. (2015) who argued that weak remnant stable stratification therein could  
 264 cause a faster decrease of  $\varepsilon$  with  $\zeta$  compared to an inverse-distance decay of  $\varepsilon(\zeta)$  that has  
 265 been discussed in numerous publications (e.g., Sanford & Lien 1999; Lozovatsky et al., 2008;  
 266 McMillan et al, 2016) in relation to marine BBL.



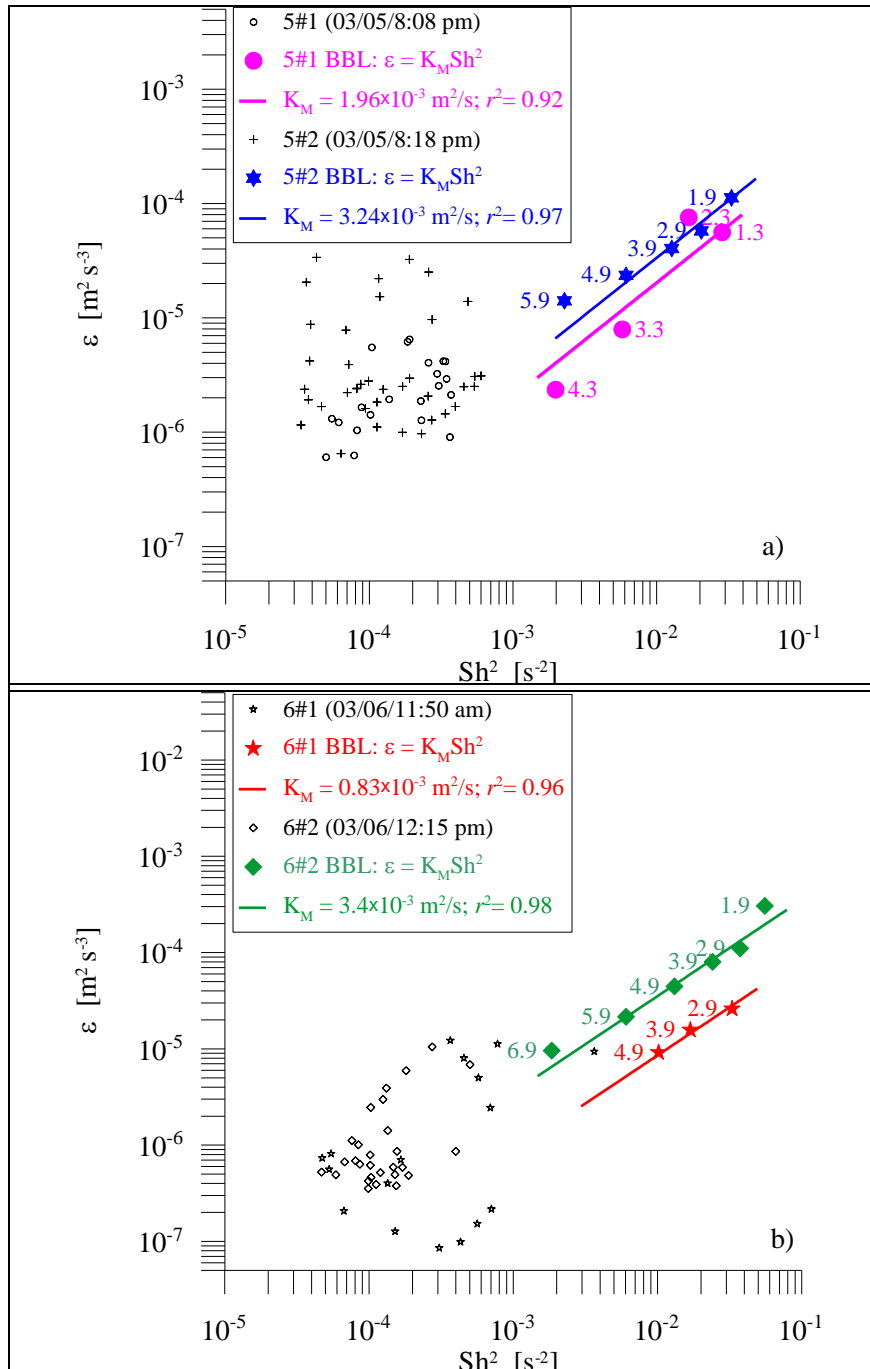
267  
 268 **Figure 6.** Examples of  $\varepsilon(\zeta)$  profiles showing an exponential increase of  $\varepsilon$  in the BBL toward the  
 269 seafloor at two stations in the Strait (March 5#3 and March 6#2, 2019) and typical  $\varepsilon(\zeta)$  profiles  
 270 measured in shallow tidal seas that exhibit exponential dependences  $\varepsilon(\zeta) \sim \varepsilon_b \exp(-\zeta/\Lambda)$  in BBL. Here,  
 271  $\varepsilon_b$  is a dissipation rate near the bottom and  $\Lambda$  a characteristic length-scale of BBL turbulence. Those  
 272 data have been reported by Lozovatsky et al. (2017a) for North Carolina shelf (NC shelf) and by  
 273 Lozovatsky et al (2012, 2015) for Changjiang River Diluted Waters (YS-CDW) in the southwestern  
 274 sector of Yellow Sea, and for the IEODO region (YS-IEODO) in the southeastern YS, respectively.  
 275 Parameters pertinent to the exponential approximations  $\varepsilon(\zeta)$  (straight lines) are in the legend.

276 While such an assumption for the MS BBL with very small  $N^2 \approx 10^{-7} - 10^{-6} \text{ s}^{-2}$  should be  
 277 considered with circumspection, Sakamoto & Akitomo (2006) argued that even weakly stable  
 278 stratification on the order of  $N^2 \approx 10^{-6} \text{ s}^{-2}$  may suppress BBL mixing specifically at high  
 279 latitudes. Rotation of tidal flow may also have a stabilizing effect on BBL turbulence, similar to  
 280 stable stratification and/or the Coriolis forces (e.g., Sakamoto & Akitomo 2008; Yoshikawa et al.  
 281 2010). Tidal ellipses in the SA region are so narrow (Figure 2b), however, that the flow  
 282 resembles a reversing rather than a rotating tide.

283 Thus, the exponential behavior of  $\varepsilon(\zeta)$  in the MS BBL as well as in several tidal  
 284 shallow seas could be considered to have different dynamics than log-layer boundary turbulence.  
 285 The clue is the exponential increase of mean squared shear in the BBL, which was presented as  
 286 an example for one of the stations in Figure 4. To verify the dependence between shear and  
 287 dissipation rate, we plotted  $\varepsilon$  vs.  $Sh^2$  for MS stations with  $z_b < 49 \text{ m}$ , where both VMP and  
 288 ADCP returned data close to the seafloor (1.3 – 2.9 mab). The data from “exponential BBLs” are  
 289 shown in Figure 7 by large symbols with adjacent numbers indicating the height from the  
 290 seafloor. If turbulence is solely generated by mean shear, for stationary turbulence the production  
 291  $K_M Sh^2$  term is balanced by viscous dissipation  $\varepsilon$  as

$$292 \quad K_M Sh^2 = \varepsilon, \quad (2)$$

293 where  $K_M$  is the eddy viscosity that parametrizes the vertical momentum flux  $\overline{u'w'} = -K_M Sh$ .  
 294 In Figure 7, the success of Eq.2 as an approximate empirical regression between  $\varepsilon$  and  $Sh^2$  in  
 295 the BBLs is apparent with high coefficients of determination  $r^2 = 0.92 - 0.98$ . The result signifies  
 296 that in the MS BBL (at  $\zeta > \sim 2 \text{ mab}$ ), the eddy viscosity  $K_M$  is independent of  $\zeta$  (constant  
 297 with height), varying in a relatively narrow range  $K_M = (0.83 - 3.4) \times 10^{-3} \text{ m}^2 \text{ s}^{-1}$ , though it  
 298 depends on the location in the Strait and the time of measurement (i.e., tidal phase); also see  
 299 Ross et al. (2019) who reported substantial tidal variability of  $K_M$  in a coastal plain estuary in  
 300 the French Atlantic Coast. Note that on March 5 and March 6, the VMP measurements were  
 301 taken in approximately the same transitional phase between low and high tide indicated in Figure  
 302 2.



303

304 **Figure 7.** The TKE dissipation rate  $\varepsilon$  vs. the squared vertical shear  $Sh^2$ : a) - stations 5#1 and 5#2, b) -  
 305 stations 6#1 and 6#2. Colored symbols belong to BBLs (see examples in Figures 4 and 6); the numbers  
 306 adjacent to the symbols specify the height above the bottom in mab. Parameters pertinent to the  
 307 approximations by Eq.2 (eddy viscosity and  $r^2$ ) are in the legend.

308

309 The estimates of  $K_M$  allow assessing the possible thickness of the turbulent BBL  $h_{tbl}$  over  
 310 a bottom roughness. Yoshikawa et al. (2010) suggested that rotating tidal currents over a large  
 311 continental shelf affect the thickness of the Ekman BBL. Considering, however, that background  
 312 rotation associated with strong reversing tidal currents is negligible in such narrow channels as  
 313 SA, it is not possible to use the classical Ekman BBL height formulae in this case (Pedlosky  
 314 1987), but analogous to the Stokes oscillatory boundary layer (e.g., Krstic & Fernando, 2001),  
 315 thickness of the reversing tidal turbulent BBL  $h_{tbl}$  over rough bathymetry composed of hard  
 316 substratum (Simeoni et al., 1997) can be written as

$$317 \quad h_{tbl} = \left( \frac{2K_M}{\omega_{td}} \right)^{1/2}, \quad (3)$$

318 where  $\omega_{td} = 1.41 \times 10^{-4} \text{ s}^{-1}$  the semidiurnal tidal frequency. Using the estimates for the present  
 319 case  $K_M = (0.83 - 3.4) \times 10^{-3} \text{ m}^2\text{s}^{-1}$ ,  $h_{tbl}$  is found to be in the range 3.5 – 6.9 m. This is in general  
 320 agreement with data shown in Figure 7, where the height of the “exponential BBL” varies  
 321 between 4.3 and 6.9 mab. Thus, reversing tidal currents in a channel of the ilk of SA may create  
 322 a specific regime of strong ( $\varepsilon_b \sim 10^{-3} \text{ Wkg}^{-1}$ ) bottom-generated turbulence, which can be  
 323 characterized by a constant eddy viscosity and a TKE dissipation rate that exponentially decays  
 324 toward the water interior. The upper boundary of the exponential decay region of turbulence in  
 325 the northern MS is 4 - 7 mab for a transitional tidal phase, characterized by a characteristic tidal  
 326 velocity  $\sim 1 \text{ ms}^{-1}$  and eddy viscosity  $\sim 10^{-3} \text{ m}^2\text{s}^{-1}$ .

#### 327 **4 Summary**

328 First ever measurements of turbulence in the northeastern Strait of Magellan were taken  
 329 during March 2 – 6, 2019. A vertical microstructure profiler (VMP) and a shipboard acoustic  
 330 Doppler current profiler (ADCP) were used to obtain estimates of the TKE dissipation rate and  
 331 vertical shear at several stations (the bottom depth ranged between 25 and 55 m), respectively, in  
 332 the Segunda Angostura region to the north of Punta Arenas. During the field campaign, tidal  
 333 elevation varied in the range  $\pm \sim 1.5 \text{ m}$ . At the time of microstructure measurements, the speed  
 334 of reversing tidal currents was 0.8 - 1.2  $\text{ms}^{-1}$ . After a mild storm, entire water column became  
 335 well mixed with the median TKE dissipation rate above the bottom boundary layer  
 336  $\varepsilon_{med}^{MS} = 1.2 \times 10^{-6} \text{ Wkg}^{-1}$ , which was about an order of magnitude higher compared to the surface

337 mixed layer turbulence measured under moderate winds in typical ocean. This was associated  
338 with strong,  $(1-2) \times 10^{-2} \text{ s}^{-1}$ , vertical shear in the water interior that yielded gradient Richardson  
339 numbers  $Ri < 10^{-1} - 10^{-2}$ , which is well below the lower critical value threshold favorable for  
340 shear-induced turbulence. The dissipation rate near the seabed in MS was close to  $\varepsilon_b \approx 10^{-3}$   
341  $\text{Wkg}^{-1}$ . Note that Thomson et al. (2012) reported the tidally-induced near-bottom dissipation rate  
342 in the Puget Sound, WA, USA, which was as high as that measured in the Strait of Magellan,  
343 namely  $\varepsilon_b \sim 10^{-4} - 10^{-3} \text{ Wkg}^{-1}$ . During microstructure measurements, the tidal-current generated  
344 turbulent BBL height was  $\sim 4 - 7 \text{ m}$ , with an exponential decay of the dissipation rate and the  
345 vertical shear toward the water interior. In the exponentially varying regime, the eddy viscosity  
346 was found to be  $K_M = (0.83 - 3.4) \times 10^{-3} \text{ m}^2\text{s}^{-1}$ , independent of the vertical coordinate  $\zeta$  but  
347 dependent on tidal phase and location. Note that the eddy viscosity as high as  $10^{-2} - 10^{-1} \text{ m}^2\text{s}^{-1}$   
348 has been reported by Ross et al. (2019) for the spring tide in a plain estuary on the French  
349 Atlantic Coast. The results of the pilot field campaign described in this paper provided first yet  
350 limited information on the specifics of turbulence in the Magellan Strait, calling for further  
351 comprehensive investigations.

## 352 **Acknowledgements**

353 We are greatly thankful to the crew of the vessel Marypaz II for immense help during the VMP  
354 measurements. The research cruise was funded by the Marine Energy Research & Innovation  
355 Center of Chile (MERIC), CORFO project 14CEI2-28228. Chilean scientists were supported by  
356 MERIC and Research Internationalization Grant of the Pontificia Universidad Católica de Chile  
357 (grant no. PUC1566). The University of Notre Dame participants were partially supported  
358 through the 2018-2019 Luksic Family Collaboration Grant Award  
359 ([https://international.nd.edu/faculty-research/grants-and-funding/luksic-family-collaboration-  
360 grant/luksic-family-collaboration-grant-awardees/](https://international.nd.edu/faculty-research/grants-and-funding/luksic-family-collaboration-grant/luksic-family-collaboration-grant-awardees/)). During the preparation of this paper, Notre  
361 Dame group was supported by ONR Grants N00014-17-1-3195 (dealing with air-sea interactions  
362 with EM ducting) as well as N00014-18-1-2472 (shelf/BBL turbulence with applications to  
363 marine fog genesis).

## 364 **Conflict of Interest**

365 The authors declare no conflicts of interest relevant to this study.

366 **Data Availability Statement**

367 The data used in this paper is available upon request from the corresponding author. Data  
368 management repository available at  
369 [https://drive.google.com/drive/folders/1mVA--r4dQ9qVBgSmxNQILcQJ\\_5ypC\\_93?usp=sharing](https://drive.google.com/drive/folders/1mVA--r4dQ9qVBgSmxNQILcQJ_5ypC_93?usp=sharing)

370  
371 **References**

- 372 Acevedo, J., Plana, J., Aguayo-Lobo, A., & Pastene, L. A. (2011). Surface feeding behavior of  
373 humpback whales in the Magellan Strait. *Revista de Biología Marina y Oceanografía*  
374 *46(3)*, 483-490. <http://dx.doi.org/10.4067/S0718-19572011000300018>
- 375 Brun, A.A., Ramirez, N., Pizarro, O., & Piola, A.R. (2020). The role of the Magellan Strait on  
376 the southwest South Atlantic shelf. *Estuarine, Coastal and Shelf Science* *237* (2020)  
377 106661, 1-11. <https://doi.org/10.1016/j.ecss.2020.106661>
- 378 Garreaud, R., Lopez, P., Minvielle, M., & Rojas, M. (2013). Large-scale control on the  
379 Patagonian climate. *Journal of Climate*, *26(1)*, 215-230.
- 380 Goodman, L., Levine, E.R., & Lueck, R.G. (2006). On measuring the terms of the turbulent  
381 kinetic energy budget from an AUV. *Journal of Atmospheric and Oceanic Technology*, *23*,  
382 977–990. <http://journals.ametsoc.org/doi/abs/10.1175/JTECH1889.1>
- 383 Guerra, M., & Thomson, J. (2017). Turbulence measurements from five-beam acoustic doppler  
384 current profilers. *Journal of Atmospheric and Oceanic Technology*, *34*, 1267–1284.  
385 <https://doi.org/10.1175/JTECH-D-16-0148.1>
- 386 Horwitz, R., & Hay, A. (2017). Turbulence dissipation rates from horizontal velocity profiles at  
387 mid-depth in fast tidal flows. *Renewable Energy*, *114*, 283–296,  
388 doi:10.1016/j.renene.2017.03.062
- 389 Jinadasa, S.U.P., Lozovatsky, I., Planella-Morató, J., Nash, J.D., MacKinnon, J.A., Lucas, A.J.,  
390 Wijesekera, H.W., & Fernando, H.J.S. (2016). Ocean turbulence and mixing around Sri  
391 Lanka and in adjacent waters of the northern Bay of Bengal. *Oceanography* *29*, 170–179.  
392 <http://dx.doi.org/10.5670/oceanog.2016.49>
- 393 Krstic, A., & Fernando, H.J.S. (2001). The nature of rough-wall oscillatory boundary layers. *J*  
394 *Hydraulic Research*, *39(6)*, 655-666. <https://doi.org/10.1080/00221686.2001.9628294>

395 Lozovatsky, I.D., Liu, Z., Hao, W., & Fernando, H.J.S. (2008). Tides and mixing in the  
396 northwestern East China Sea. Part II: The near-bottom turbulence. *Continental Shelf*  
397 *Research*, 28(2), 338-350. doi:10.1016/j.csr.2007.08.007

398 Lozovatsky, I., Liu, Z., Fernando, H.J.S., Armengol, J., & Roget, E. (2012). Shallow water tidal  
399 currents in close proximity to the seafloor and boundary-induced turbulence. *Ocean*  
400 *Dynamics*, 62, 177-201. doi:10.1007/s10236-011-0495-3.

401 Lozovatsky, I., Lee, J.-H., Fernando, H.J.S., Kang, S.K., & Jinadasa, S.U.P. (2015). Turbulence  
402 in the East China Sea: The summertime stratification. *Journal Geophysical Research:*  
403 *Oceans*, 120, 1856–1871. doi: 10.1002/2014JC010596

404 Lozovatsky, I., Planella-Morato, J., Shearman, K., Wang, Q., & Fernando, H.J.S. (2017a). Eddy  
405 diffusivity and elements of mesoscale dynamics over North Carolina shelf and contiguous  
406 Gulf Stream waters. *Ocean Dynamics* 67, 783-798. doi 10.1007/s10236-017-1059-y

407 Lozovatsky, I., Fernando, H.J.S., Planella-Morato, J., Liu, Z., Lee, J.-H., & Jinadasa, S.U.P.  
408 (2017b). Probability distribution of turbulent kinetic energy dissipation rate in ocean:  
409 Observations and approximations. *Journal Geophysical Research: Oceans* 122, 8293-  
410 8308. doi 10.1002/2017JC013076

411 Lozovatsky I., Pirro, A., Jarosz, E., Wijesekera, H.W., Jinadasa, S.U.P., & Fernando, H.J.S.  
412 (2019). Turbulence at the periphery of Sri Lanka dome. *Deep Sea Research II*, 168,  
413 104614:1-8. <https://doi.org/10.1016/j.dsr2.2019.07.002>

414 Lozovatsky, I., C. Wainwright, E. Creegan, and H. J. S. Fernando, 2021: Ocean turbulence and  
415 mixing near the shelf break southeast of Nova Scotia. *Boundary-Layer Meteor.* **181**, 425-  
416 441. <https://doi.org/10.1007/s10546-020-00576-z>

417 Lutz, V., Frouin, R., Negri, R., Silva, R., Pompeu, M., Rudorff, N., Cabral, A., Dogliotti, A., &  
418 Martinez, G. (2016). Bio-optical characteristics along the Straits of Magallanes.  
419 *Continental Shelf Research* 119, 56–67.

420 McMillan, J.M., Hay, A.E., Lueck, R.G., & Wolk, F. (2016). Rates of dissipation of turbulent  
421 kinetic energy in a high Reynolds number tidal channel. *Journal Physical Oceanography*,  
422 33, 817–837, doi:10.1175/JTECH-D-15-0167.1

423 McMillan, J.M., & Hay, A.E. (2017). Spectral and structure function estimates of turbulence  
424 dissipation rates in a high-flow tidal channel using broadband ADCPs. *Journal of*  
425 *Atmospheric and Oceanic Technology*, 34, 5–20, doi:10.1175/JTECH-D-16-0131.1.

426 Medeiros, Carmen & Bjorn Kjerfve. (1988). Tidal characteristics of the Strait of Magellan.  
427 *Continental Shelf Research*, 8(8), 947-960.

428 Monin, A.S., & Yaglom, A.M. (1971). Statistical Fluid Mechanics: Mechanics of Turbulence, 1.  
429 MIT Press, Cambridge, MA, 782pp.

430 Pedlosky, J. (1987). *Geophysical Fluid Dynamics*. 2d ed. Springer-Verlag, 710 pp.  
431 <https://doi.org/10.1007/978-1-4612-4650-3>

432 Ross, L., Huguenard, K., & Sottolichio, A. (2019).: Intratidal and fortnightly variability of  
433 vertical mixing in a macrotidal estuary: The Gironde. *Journal of Geophysical Research:*  
434 *Oceans*, 124, 2641–2659. <https://doi.org/10.1029/2018JC014456>

435 Roget, E., Lozovatsky, I., Sanchez, X., & Figueroa, M. (2006). Microstructure measurements in  
436 natural waters: Methodology and applications. *Progress in Oceanography* 70, 123-148.

437 Sakamoto, K., & Akitomo, K. 2006: Instabilities of the tidally induced bottom boundary layer in  
438 the rotating frame and their mixing effect. *Dynamics of Atmospheres and Oceans* 41, 191–  
439 211.

440 Sanford, T.S., and Lien, R.-C. (1999). Turbulent properties in a homogeneous tidal boundary  
441 layer. *Journal of Geophysical Research: Oceans* 104, (C1), 1245–1257.

442 Simeoni, U., Fontolan, G., & Colizza, E. (1997). Geomorphological characterization of the  
443 coastal and marine area between Primera and Segunda Angostura, Strait of Magellan  
444 (Chile) *Journal of Coastal Research*, 13, No.3, 916-924.

445 St. Laurent, L.C., Simmons, H.L., & Jayne, S.R. (2002). Estimating tidally driven mixing in the  
446 deep ocean, *Geophysical. Research Letters* 29(23), 2106, doi:10.1029/2002GL015633

447 Thomson, J., Polagye, B., Durgesh, V., & Richmond, M.C. (2012). Measurements of turbulence  
448 at two tidal energy sites in Puget Sound, WA, *IEEE Journal of oceanic engineering*, 37(3),  
449 363-374

450 Yoshikawa, Y., Endoh, T., Matsuno, T., Wagawa, T., Tsutsumi, E., Yoshimura, H., & Morii, Y.  
451 (2010). Turbulent bottom Ekman boundary layer measured over a continental shelf.  
452 *Geophysical. Research Letters* 37, L15605. doi: 10.1029/2010GL044156

453 Wolk, F. & Lueck, R. (2012). VMP turbulence profiler measurements in a tidal channel.  
454 *Rockland Technical Note 024*. 2012-06-30. [https://rocklandscientific.com/wp-](https://rocklandscientific.com/wp-content/uploads/2021/12/TN_024_VMP_in_Tidal_Channels.pdf)  
455 [content/uploads /2021/12/TN\\_024\\_VMP in Tidal Channels.pdf](https://rocklandscientific.com/wp-content/uploads/2021/12/TN_024_VMP_in_Tidal_Channels.pdf)

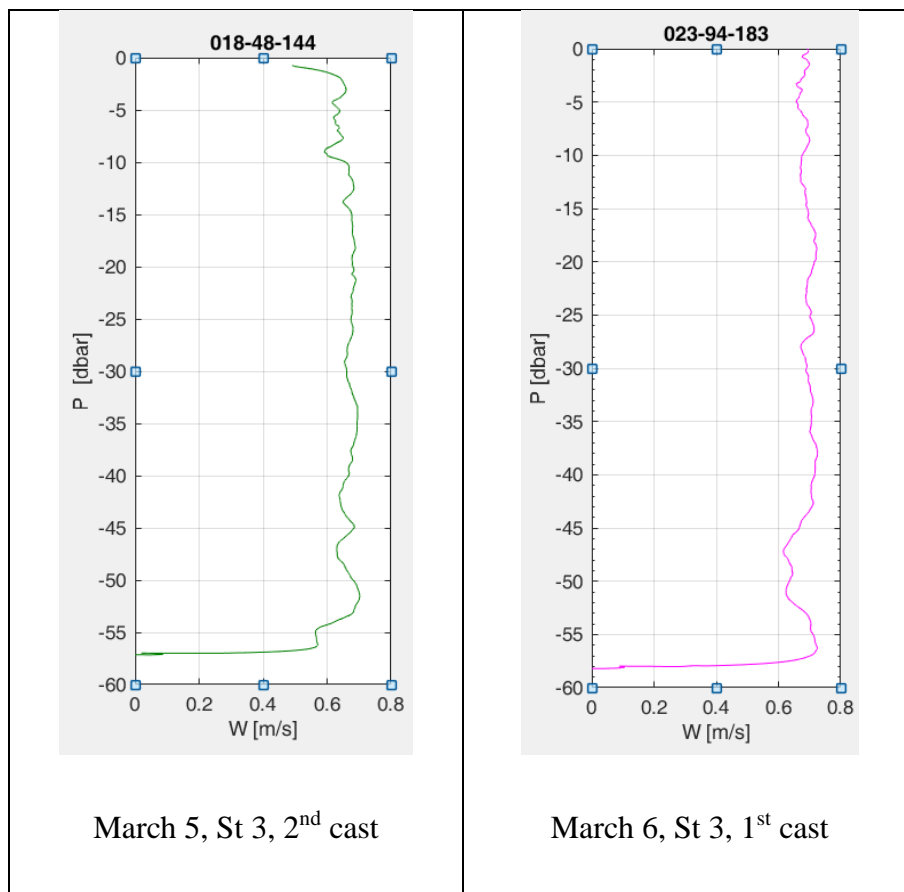
456

457

458 **Appendix**

459 Examples of the VMP sinking velocity profiles  $W(P)$  shown in Fig. A1 indicate fairly  
460 undisturbed almost constant  $W(P) \sim 0.7$  m/s during a major portion of the casts and a sharp drop of  
461  $W(P)$  to zero at the end of the casts ( $P$  is pressure).

462



463 **Figure A1.** The VMP sinking velocity profiles for two casts taken in the Magellan Strait on March 5 and  
464 6, 2019 (see stations in Figure 1).

# A Snapshot of Turbulence in the Northeastern Strait of Magellan

I. D. Lozovatsky<sup>1</sup>, C. Escauriaza<sup>3</sup>, L. Suarez<sup>3,4</sup>, H. J. S. Fernando<sup>1,2</sup>, M. E. Williams<sup>5</sup>, R. S. Coppersmith<sup>1</sup>, and N. Mayorga<sup>3</sup>

<sup>1</sup>Department of Civil & Environmental Engineering & Earth Sciences, University of Notre Dame, USA

<sup>2</sup>Department of Aerospace and Mechanical Engineering, University of Notre Dame, USA

<sup>3</sup>Departamento de Ingeniería Hidráulica y Ambiental. Pontificia Universidad Católica de Chile, Chile

<sup>4</sup>Marine Energy Research & Innovation Center (MERIC), Santiago, Chile.

<sup>5</sup>Departamento de Obras Civiles. Universidad Técnica Federico Santa María, Valparaíso, Chile

Corresponding author Iossif Lozovatsky ([i.lozovatsky@nd.edu](mailto:i.lozovatsky@nd.edu))

## Key Points:

- Results of first ever direct measurements of small-scale turbulence in the Strait of Magellan conducted using a microstructure profiler VMP-500 are reported.
- Above the bottom boundary layer, the probability distribution of turbulent kinetic energy (TKE) dissipation rate was lognormal with a median exceeding  $10^{-6} \text{ Wkg}^{-1}$ .
- In the BBL, the mean shear and TKE dissipation rate decreased exponentially with the distance from the seafloor  $\zeta$  leading to an eddy viscosity  $\sim 10^{-3} \text{ m}^2\text{s}^{-1}$  independent on  $\zeta$ .

## 29 **Abstract**

30 First-ever measurements of the turbulent kinetic energy (TKE) dissipation rate in the  
31 northeastern Strait of Magellan (Segunda Angostura region) taken in March 2019 are reported  
32 here. At the time of microstructure measurements, the magnitude of the reversing tidal current  
33 ranged between 0.8 and 1.2 ms<sup>-1</sup>. The probability distribution of the TKE dissipation rate in the  
34 water interior above the bottom boundary layer was lognormal with a high median value  
35  $\varepsilon_{med}^{MS} = 1.2 \times 10^{-6}$  Wkg<sup>-1</sup>. Strong vertical shear,  $(1-2) \times 10^{-2}$  s<sup>-1</sup> in the weakly stratified water  
36 interior ensued a sub-critical gradient Richardson number,  $Ri < 10^{-1} - 10^{-2}$ . In the bottom  
37 boundary layer (BBL), the vertical shear and the TKE dissipation rate both decreased  
38 exponentially with the distance from the seafloor  $\zeta$ , leading to a turbulent regime with the eddy  
39 viscosity  $K_M \sim 10^{-3}$  m<sup>2</sup>/s, which varied with the time and location, while being independent of  
40 the vertical coordinate in the upper part of BBL (for  $\zeta > \sim 2$  meters above the bottom).

## 41 **Plain Language Summary**

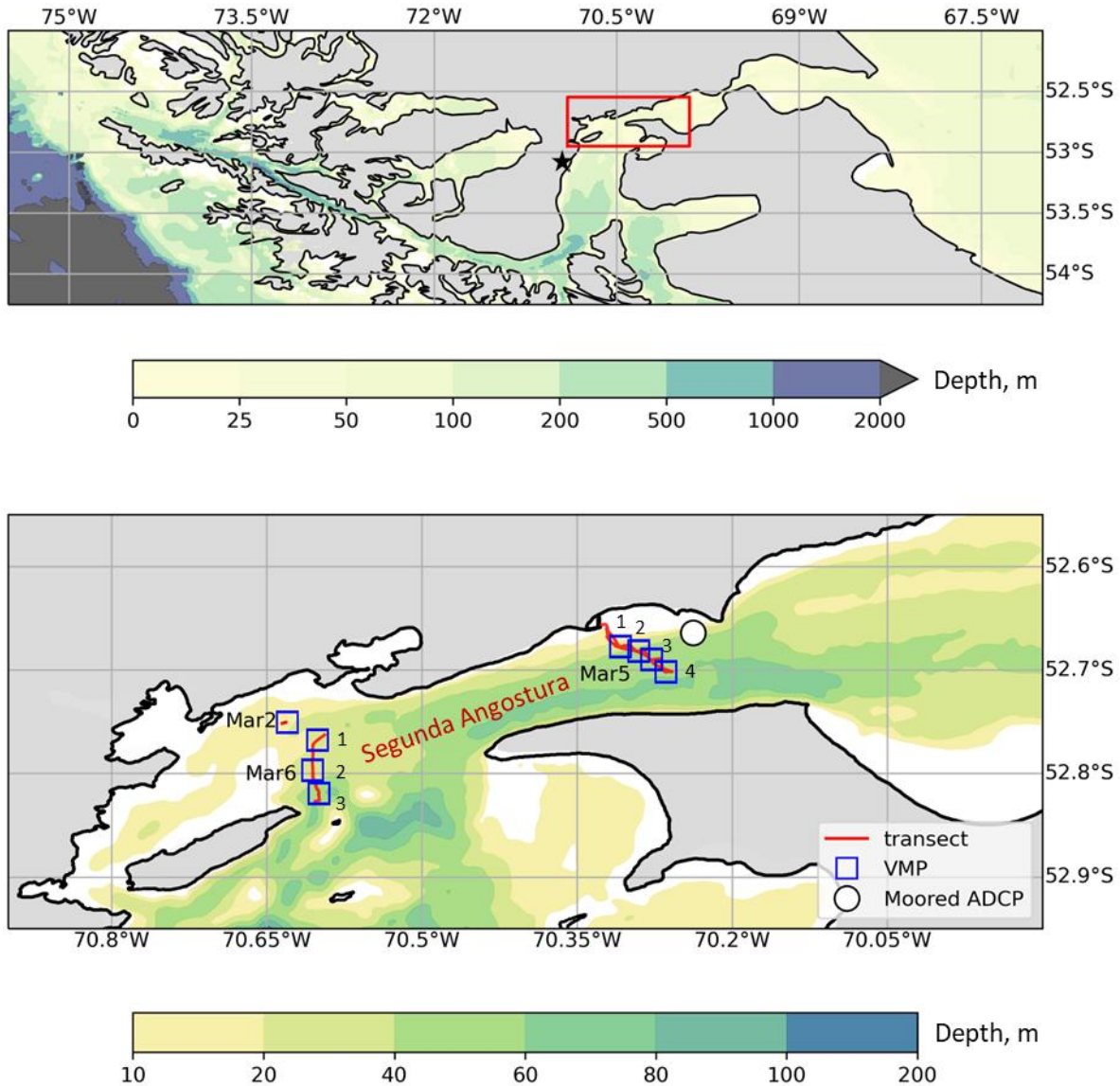
42 The Strait of Magellan (MS) is a narrow  $\sim 2$  km wide and  $\sim 500$  km long waterway that  
43 meanders between the Atlantic and Pacific oceans, separating Patagonia from Tierra del Fuego.  
44 The Strait is an environmentally unique, and undergoes rapid ecological changes due to  
45 anthropogenic stressors. To study small-scale marine turbulence in the region, which influences  
46 vertical transport of heat, momentum, nutrients, sediments and other substances, we conducted  
47 first ever direct measurements of turbulent kinetic energy (TKE) dissipation rate  $\varepsilon$  in the  
48 northeastern part of the Strait (Segunda Angostura narrow) using a vertical microstructure  
49 profiler. The most notable finding is the very high level of turbulence existing near the seafloor,  
50 signified by  $\varepsilon_b \approx 10^{-3}$  Wkg<sup>-1</sup>, which is among the highest TKE dissipation rate measured  
51 previously by numerous authors in various narrow tidal channels. Tidal currents in MS generated  
52 a turbulent bottom boundary layer (BBL) with an exponential decay of the dissipation rate and  
53 the mean velocity gradient (vertical shear) toward the water interior. This turbulent regime can  
54 be specified by the eddy viscosity on the order of  $\sim 10^{-3}$  m<sup>2</sup>/s that varied with time and location  
55 while being independent of the vertical coordinate  $\zeta$  in the upper part of BBL (for  $\zeta > \sim 2$   
56 meters above the bottom). The measurements described has only limited information on the  
57 specifics of turbulence in MS, calling for further investigations of turbulence and mixing therein.

## 58 **1 Introduction**

59           The Strait of Magellan (henceforth also the Magellan Strait (MS) or just the Strait) is an  
60 environmentally unique region being, in particular, a feeding ground to humpback whales  
61 (Acevedo et al., 2011). The region currently experiences changes of its ecological balance due to  
62 anthropogenic stressors such as excessive fishing, offshore oil production and newly leased areas  
63 for aquaculture. Understanding of small-scale dynamical processes in the Magellan Strait is  
64 paramount for multidisciplinary studies of physical, biogeochemical and ecological processes in  
65 the coastal regions of Patagonia. For this reason, we launched the first ever in-situ measurements  
66 of the kinetic energy dissipation rate in the north-eastern part of the Strait to obtain estimates of  
67 turbulence and mixing across the water column down to the bottom boundary layer (BBL).

68           The Strait of Magellan is a narrow  $\sim 1.1$  nautical miles (NM) waterway that meanders  
69 between the Atlantic and Pacific oceans, separating Patagonia from Tierra del Fuego; it is about  
70 310 NM long (Figure 1). According to Simeoni et al. (1997), the mean annual air temperature of  
71 the eastern MS is  $6 - 7^\circ \text{C}$ , varying from  $8^\circ$  to  $11^\circ \text{C}$  in the summer (December - February) and  
72 from  $2^\circ$  to  $3^\circ \text{C}$  in the winter (June-August). Easterly-directed winds of characteristic speed  $7$   
73  $\text{ms}^{-1}$  are typical in the region (Garreaud et al., 2013). Stormy winds (up to  $25 \text{ms}^{-1}$ ) are often  
74 observed during winter and spring seasons.

75           Strong barotropic tidal flow and winds are the major drivers of mesoscale circulation in  
76 the Strait. On the Atlantic side, the Strait is characterized by high-amplitude semidiurnal tides  
77 with a mean tide range of  $7.1 \text{ m}$ , which gradually decreases to about  $1.5 - 2 \text{ m}$  toward Punta  
78 Arenas (see Figure 4 of Medeiros & Kjerfve, 1988). Tidal amplification occurs in a series of  
79 narrows at the Atlantic side to the northeast of Punta Arenas (Figure 1), for example, in Segunda  
80 Angostura (SA), where our pilot field campaign was conducted (see also detailed map of SA in  
81 Figure 1 of Lutz et al., 2016). The seabed in SA is mainly composed of hard substratum and  
82 outcropping rocks (Simeoni et al., 1997). High level of tidally induced turbulence is an expected  
83 phenomenon in SA as has been reported in several recent publications on turbulence in narrow  
84 tidal channels elsewhere (e.g., McMillan et al., 2016; Horwitz & Hay, 2017; Guerra & Thomson,  
85 2017; Ross et al., 2019).



86

87 **Figure 1.** Upper panel: the measurement site (bounded by a red box) in the main passage of the Magellan  
 88 Strait to the NNE from Punta Arenas (black star). Lower panel: an enlarged section of the Magellan Strait  
 89 showing locations of the VMP stations (squares marked by the date and station numbers); the ADCP  
 90 mooring (a white circle). Two separate color palettes (scales) specify the mean water depth of the upper  
 91 and lower panels, respectively. Segunda Angostura is a narrower channel in the Atlantic sector of the  
 92 Magellan Strait.

93 Very limited information exists on hydrological characteristics of the Magellan waters.  
 94 Antezana (1999) reported basic hydrographic features (temperature and salinity) in the main  
 95 passages of the Strait and suggested that adjacent oceanic waters were warmest in the Atlantic  
 96 and saltiest in the Pacific sectors, maintaining an along-strait horizontal T-S gradient.  
 97 Precipitations and continental freshwater discharge to the Strait induce patterns of the diluted

98 near surface waters transported to the Atlantic Patagonian shelf (Brun et al., 2020). The large-  
99 scale hydrological features as well as seasonal variations of mesoscale circulation may influence  
100 turbulence in the Strait, but strong tides and local winds are the most likely generators of  
101 turbulence in the shallow Atlantic sector of the MS.

102 To shed light on characteristics of small-scale turbulence in MS, a short field campaign  
103 was carried out in the northeastern part of the Strait using a vertical microstructure profiler  
104 VMP-500 and acoustic Doppler current profilers (section 2). Patterns of tidal currents during the  
105 microstructure measurements are described in section 3.1. Sections 3.2 and 3.3 present several  
106 examples of the TKE dissipation rate profiles comparing the level of turbulence in well-mixed  
107 water interior of MS (section 3.3) with turbulence intensity (illustrated by log-normal  
108 distribution functions of the dissipation rate) of homogeneous non-stratified layers in other  
109 kindred oceanic regions. Specifics of turbulence and mean current shear profiles in the BBL of  
110 Segunda Angostura are discussed in section 3.4 vis-à-vis our own measurements carried out in  
111 various tidally affected shallow seas. The main results are summarized in section 4, including a  
112 comparison of turbulence measurements in narrow tidal channels elsewhere.

## 113 **2 Measurements**

114 Turbulence and stratification in the Strait were measured using a Vertical Microstructure  
115 Profiler, VMP-500, (<http://rocklandscientific.com/products/profilers/vmp-500/>). Airfoil probes  
116 were used to estimate small-scale shear, enabling the calculation of TKE dissipation rate  $\varepsilon(z)$ ,  $z$   
117 being the (downward) vertical coordinate. An accelerometer, pressure sensor and a SeaBird  
118 temperature-conductivity package provided precise salinity, temperature and potential density  
119 profiles. The airfoil sensors were calibrated by Rockland Scientific prior to and after the field  
120 campaign. The measurements were taken from a medium-size fishing boat, Marypaz II. The ship  
121 was equipped with A-frame at the rear deck, which was used to recover the VMP after each cast  
122 conducted in a free-falling mode with a thin tethered cable of neutral buoyancy. We were able to  
123 keep the VMP sinking velocity constant,  $W \sim 0.7 \text{ ms}^{-1}$  (see Appendix), with a sharp drop off to  
124 zero at the end of the casts (usually at  $\sim 1\text{-}2$  m above the bottom)

125 A shipboard acoustic Doppler current profiler (ADCP) measured vertical profiles of  
126 zonal  $u(z)$  or  $u(\zeta)$  and meridional  $v(z)$  or  $v(\zeta)$  velocity components. Here, the distance

127 from the sea surface  $z$ ,  $\zeta = z_b - z$  is a distance from the sea floor in meters above the bottom  
128 (mab) and  $z_b$  is the bottom depth in point at the time of measurements. A Teledyne Workhorse  
129 sentinel ADCP operated at 600 kHz with high vertical resolution (1-m bin size), but the  
130 measurements were restricted to the depth range  $z = 1 - 49$  m. Processing of the VMP and ADCP  
131 data followed well-established methodology adopted during our previous field campaigns (e.g.,  
132 Lozovatsky et al., 2019, 2021; see also Roget et al., 2006 and Goodman et al., 2006). Multiple  
133 GPS systems were on board, but an automatic weather station was not present; thus, the  
134 meteorological conditions at Punta Arenas during the cruise were used as local.

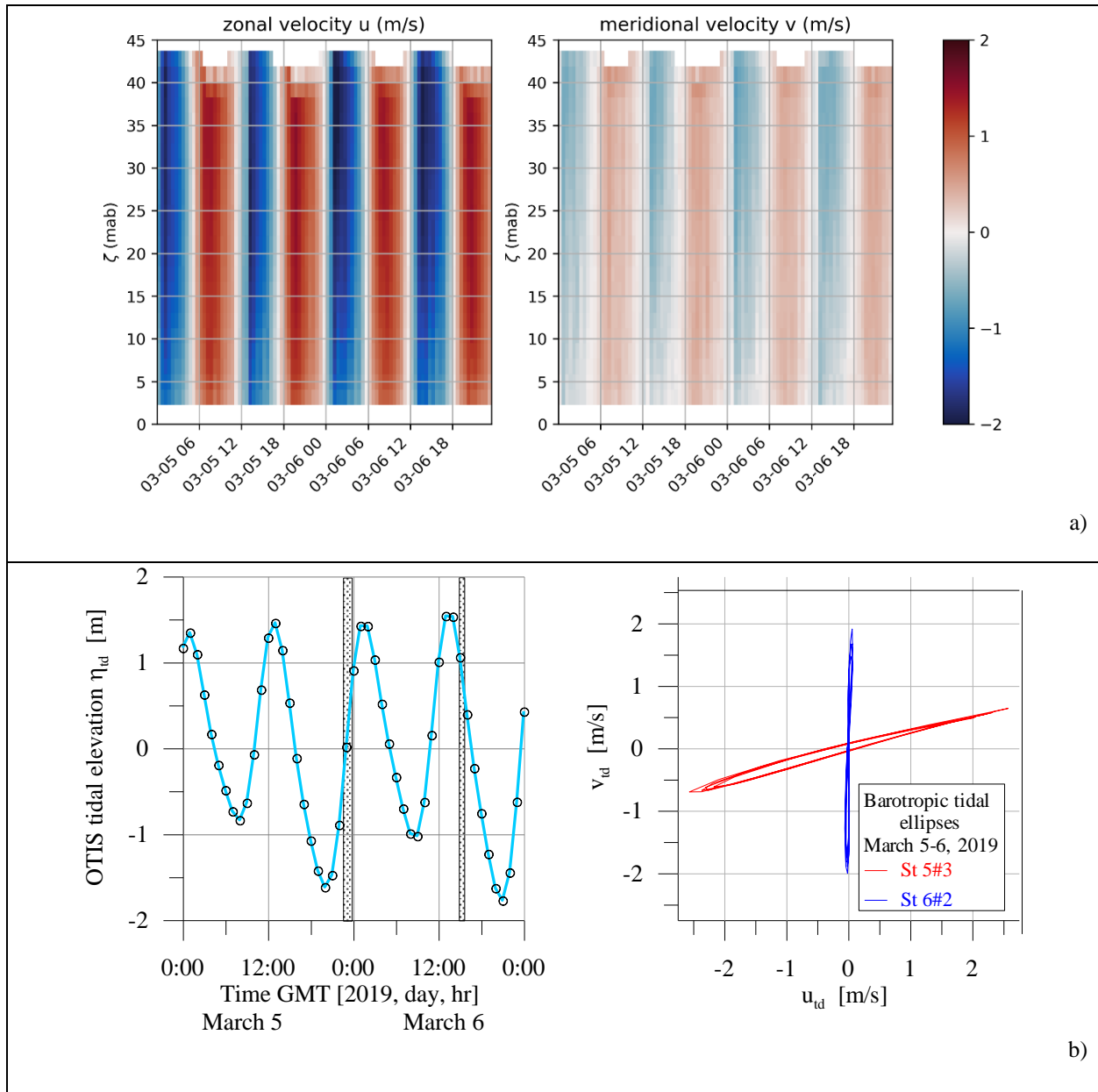
135 The VMP-500 was successfully deployed at eight stations near the eastern and western  
136 ends of Segunda Angostura (SA) of the Magellan Strait (Figure 1). The first test station was  
137 taken on March 2 near the coast (the bottom depth  $z_b \sim 21$  m) under calm weather conditions  
138 (wind speed 2-3  $\text{ms}^{-1}$ ). This appears to be the only VMP station wherein a weak but  
139 distinguishable temperature, salinity and density stratifications of the water column were  
140 observed. On March 3, a bottom-mounted ADCP mooring was setup in the northern part of SA  
141 (see Figure 1), but the VMP measurements on March 3 and 4 were suspended due to rough seas  
142 (wave height up to 2 m) and high winds that periodically exceeded 10-12  $\text{ms}^{-1}$ . Toward the end  
143 of the day of March 5 the stormy wind ceased, permitting to conduct four VMP stations in the  
144 central part of SA (closer to its eastern entrance,  $\varphi = 52^\circ 39'58'' - 52^\circ 42'7''$  S,  $\lambda = 70^\circ 19'0'' -$   
145  $70^\circ 15'51''$  W; with  $z_b$  varying from 30 to 57 m). The measurements continued on March 6 at  
146 three stations across the Strait about four miles to the west off the western SA entrance ( $\varphi =$   
147  $52^\circ 53'54'' - 52^\circ 49'5''$  S,  $\lambda = 70^\circ 49'59'' - 70^\circ 38'58''$  W with  $z_b$  varying from 26 to 57 m).  
148 Positions of all VMP stations are shown in Figure 1.

### 149 **3 Results**

#### 150 **3.1 Tidal flow**

151 Basic tidal characteristics in the SA area of MS are given in Figure 2 for two main days of  
152 VMP measurements (March 5-6, 2019). The ADCP current components  $u(\zeta, t)$  and  $v(\zeta, t)$  at  
153 the mooring location are shown in Figure 2a and the tidal elevation  $\eta_{td}(t)$  and tidal ellipses are  
154 in Figure 2b. It appears that a semidiurnal tide ( $\omega_{td} = 1.41 \times 10^{-4} \text{ s}^{-1}$ ) with current amplitude  $\sim 2$

155  $\text{ms}^{-1}$  and surface elevation  $\sim 1.5$  m was a dominant background force governing mean currents  
 156 that generated small-scale turbulence in the SA region. The tidal ellipses (Figure 2b) are highly  
 157 stretched in NE-SW direction along the SA axis in the middle of the narrow channel.



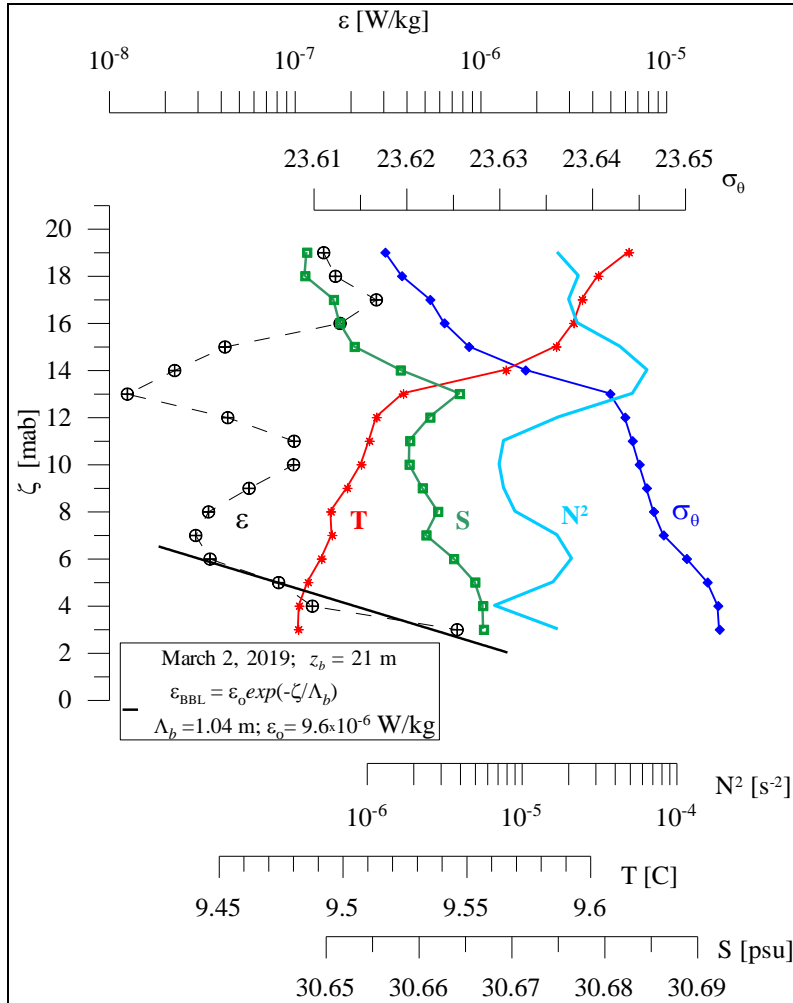
158 **Figure 2.** a) - ADCP current components at the mooring location (see Figure 1) for March 5-6, 2019  
 159 (color scale in  $\text{ms}^{-1}$ ; b) left - tidal elevation in SA based on modeling data of OTIS (OSU Tidal Inversion  
 160 Software, courtesy of S. Erofeeva; <https://www.tpxo.net/otis>). Periods of VMP measurements are marked  
 161 by grey segments; b) right – OTIS barotropic tidal ellipses in SA for St.5#3 and St. 6#2.

162 To the west of SA, the dominant tidal current was in the S-N direction with a large  
 163 amplitude meridional component ( $v_{tid} \approx \pm 2 \text{ ms}^{-1}$ ) and a very small zonal component ( $u_{tid} \approx \pm 0.07$

164  $\text{ms}^{-1}$ ). Note that the VMP measurements were taken during rising tide on March 5 and during  
 165 subsiding tide on March 6, both not at the periods of maximum tidal velocities due to the  
 166 operational constrains.

### 167 3.2 MS turbulence: stable ambient stratification

168 Figure 3 shows the TKE dissipation rate profile  $\varepsilon(\zeta)$  obtained on March 2 at the  
 169 beginning of field campaign under light winds ( $2\text{-}3 \text{ms}^{-1}$ ).



170  
 171 **Figure 3.** Profiles of the TKE dissipation rate  $\varepsilon(\zeta)$ , temperature  $T(\zeta)$ , salinity  $S(\zeta)$ , potential  
 172 density  $\sigma_\theta(\zeta)$ , and squared buoyancy frequency  $N^2(\zeta)$  observed under light winds to the west from  
 173 SA. Here  $\zeta$  is the distance above the bottom in meters (mab).

174 The background density stratification was characterized by  $N^2 \sim 2 \times 10^{-5} \text{ s}^{-2}$  for the upper  
 175 weakly stratified 5 meters of the water column ( $\zeta > 16$  mab), increasing to  $\sim 6 \times 10^{-5} \text{ s}^{-2}$  in a

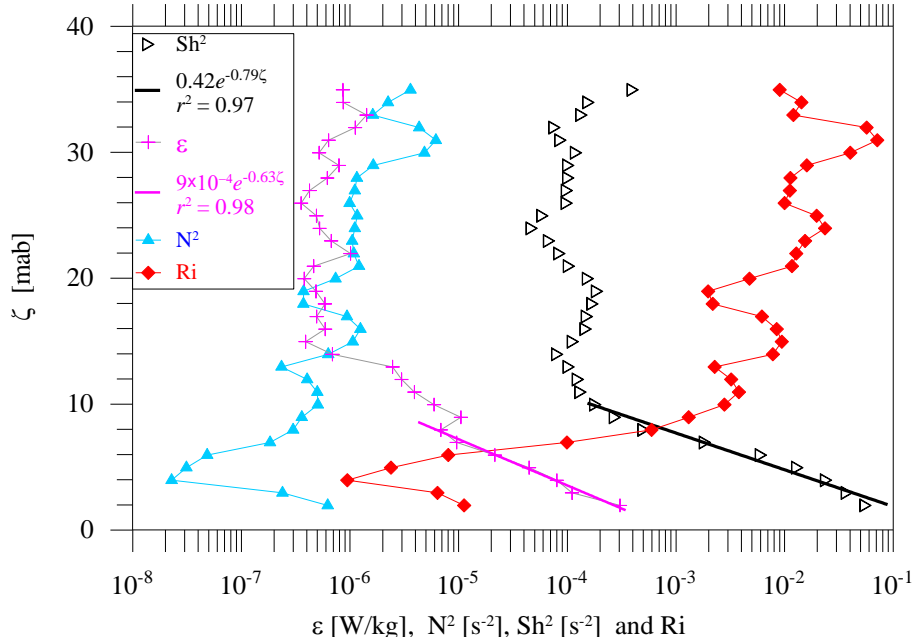
176 narrow,  $\zeta = 13 - 16$  mab, pycnocline (thermocline). Then it generally decreased to  
 177  $N^2 \sim (0.9 - 2) \times 10^{-5} \text{ s}^{-2}$  below the pycnocline ( $\zeta < 11 - 12$  mab). The TKE dissipation rate profile  
 178 shows relatively high  $\varepsilon \approx (1 - 2) \times 10^{-7} \text{ Wkg}^{-1}$  in the near surface layer, decreasing to  $\varepsilon \sim 10^{-8}$   
 179  $\text{Wkg}^{-1}$  in the pycnocline. Starting from  $\zeta \sim 6$  mab, however,  $\varepsilon(\zeta)$  clearly exhibited an  
 180 exponential growth toward the seafloor (black line in Figure 3), reaching  $\varepsilon \sim 8 \times 10^{-7} \text{ Wkg}^{-1}$  at  $\zeta$   
 181  $\sim 3$  mab. Note that at this shallow station the VMP did not descend closer to the bottom, where  $\varepsilon$   
 182 could perhaps rise by another order of magnitude. The TKE dissipation in the interior of stratified  
 183 water column,  $\varepsilon \sim (1 - 3) \times 10^{-8} \text{ Wkg}^{-1}$ , appears to be comparable with (but at the higher end of)  
 184 the dissipation estimates obtained in our previous measurements on shallow stratified *tidal* shelves  
 185 elsewhere (see  $\varepsilon(\zeta)$  profiles presented later in Figure 6). Note that even in narrow tidal channels  
 186 (e.g., Sansum Narrows, which separates Vancouver and Saltspring Islands in British Columbia,  
 187 Canada; flooding tide of  $\sim 2 \text{ ms}^{-1}$ ) turbulence is strongly affected by layers of stable stratification,  
 188 dropping  $\varepsilon < 10^{-8} \text{ Wkg}^{-1}$  (Wolk & Lueck, 2012).

### 189 **3.3 MS turbulence: well-mixed water interior**

190 After stormy winds ( $10\text{-}12 \text{ ms}^{-1}$ ) on March 4, the water column in SA was almost  
 191 completely mixed, being characterized by very low buoyancy frequency  $N^2$  in the range  
 192  $2 \times (10^{-7} - 10^{-6}) \text{ s}^{-2}$ . Figure 4 shows vertical profiles of  $N^2(\zeta)$ ,  $Sh^2(\zeta)$  (the squared vertical  
 193 shear, ship-based ADCP measurements), the gradient Richardson number  
 194  $Ri(\zeta) = N^2(\zeta)/Sh^2(\zeta)$  and  $\varepsilon(\zeta)$  to demonstrate properties of well-mixed tidal flow in the  
 195 MS. Vertical structure of all variables in Figure 4 consists of two distinct layers. The first is the  
 196 bottom boundary layer, where the dissipation rate exponentially increases with depth (  
 197  $\zeta < \zeta_{BBL} \approx 8$  mab) mirroring an exponential increase of vertical shear and corresponding  
 198 decrease of  $Ri(\zeta)$ . Although  $N^2(\zeta)$  shows slight increase in two meters just above the  
 199 seafloor, the values of  $N^2 < 7 \times 10^{-7} \text{ s}^{-2}$  are still extremely low.

200 Another major layer covers the water column above the BBL ( $\zeta > \zeta_{BBL}$ ), where the shear  
 201 and the dissipation rate vary around the means  $\langle \varepsilon \rangle = 6.8 \times 10^{-7} \text{ Wkg}^{-1}$  and  $\langle Sh^2 \rangle = 1.1 \times 10^{-4} \text{ s}^{-2}$

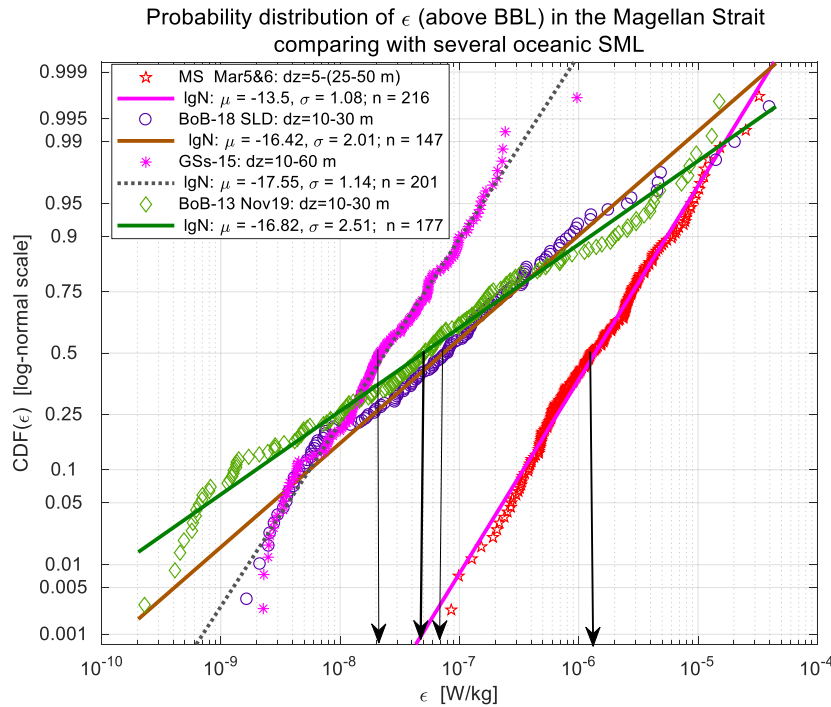
202 for an example in Figure 4. Statistical behavior of such random variable as  $\varepsilon$  can be specified in  
 203 terms of the cumulative probability distribution function  $CDF(\varepsilon)$ , which is shown in Figure 5  
 204 by red pentagrams, calculated using all dissipation samples pertained to the depth range between  
 205  $z_o = 5$  m and  $z_{BBL} = 25 - 50$  m depending on the BBL height  $\zeta_{BBL}$  in every specific VMP cast.  
 206



207  
 208 **Figure 4.** An example of the vertical profiles of squared buoyancy frequency  $N^2(\zeta)$ , mean shear  
 209  $Sh^2(\zeta)$ , gradient Richardson number  $Ri(\zeta)$ , and dissipation rate  $\varepsilon(\zeta)$  obtained on March 6 in the  
 210 mixed waters of MS (signified by very small values of  $N^2(\zeta)$  in the entire water column). Station 6#2  
 211 in Figure 1.

212 To compare turbulence intensity in homogeneous waters of MS with non-stratified  
 213 turbulence in oceanic regions elsewhere, Figure 5 shows several examples of  $CDF(\varepsilon)$  obtained  
 214 for surface mixed layers (SML) in the northern (Jinadasa et al., 2016) and southwestern  
 215 (Lozovatsky et al., 2019) Bay of Bengal (BoB-13 and BoB-18, respectively) and in the Gulf  
 216 Stream region (GS-15). Those  $CDF(\varepsilon)$  were calculated for  $z = 10$  to 30 m for relatively shallow  
 217 SML underlain by a sharp pycnocline in both BoB regions (moderate local winds) and  $z = 10$  to  
 218 50 m in a deep, well-developed SML for GS-15 (Lozovatsky et al., 2017a).

219 As expected, all  $CDFs(\epsilon)$  in Figure 5 are well approximated by lognormal probability  
 220 distribution of the Gurvich & Yaglom (1967) model as well as numerous data obtained in non-  
 221 stratified marine layers (e.g., Lozovatsky et al., 2017b; McMillan & Hay, 2017). Furthermore,  
 222 Figure 5 indicates that turbulence in SA is much stronger than that typically observed in oceanic  
 223 SML under similar (low and moderate) winds. The median value of the TKE dissipation rate in  
 224 the MS above the BBL  $\epsilon_{med}^{MS} = 1.2 \times 10^{-6} \text{ Wkg}^{-1}$  is an order of magnitude higher than that in the  
 225 SML  $CDFs$  shown in Figure 5, where  $\epsilon_{med}^{SML} \approx (2-7) \times 10^{-7} \text{ Wkg}^{-1}$ . Such high level of turbulence  
 226 appears to be governed by shear instability developed across the entire water column in the SA  
 227 region, where  $\langle Sh^2 \rangle = 1.1 \times 10^{-4} \text{ s}^{-2}$  and highly subcritical  $Ri$  values, varying above the BBL  
 228 mostly in the range  $Ri \sim 0.01 - 0.1$ .



229

230 **Figure 5.** Cumulative distribution functions of the dissipation rate  $CDF(\epsilon)$  for mixed water interior of  
 231 the Magellan Strait (MS 2019, March 5&6 data) and examples of  $CDF(\epsilon)$  for oceanic surface mixed  
 232 layer (SML) under light and moderate winds. Those measurements were taken in the northern and  
 233 southern Bay of Bengal (BoB-13 and BoB-18, respectively) and in the Gulf Stream (GS-15). The depth  
 234 ranges selected for  $CDF(\epsilon)$  calculation, the number of CDF samples  $n$  and parameters of lognormal  
 235 approximations of the empirical distributions  $\mu$  and  $\sigma$  are in the legend. The arrows point to the  
 236 corresponding median values.

237 **3.4 MS turbulence: BBL**

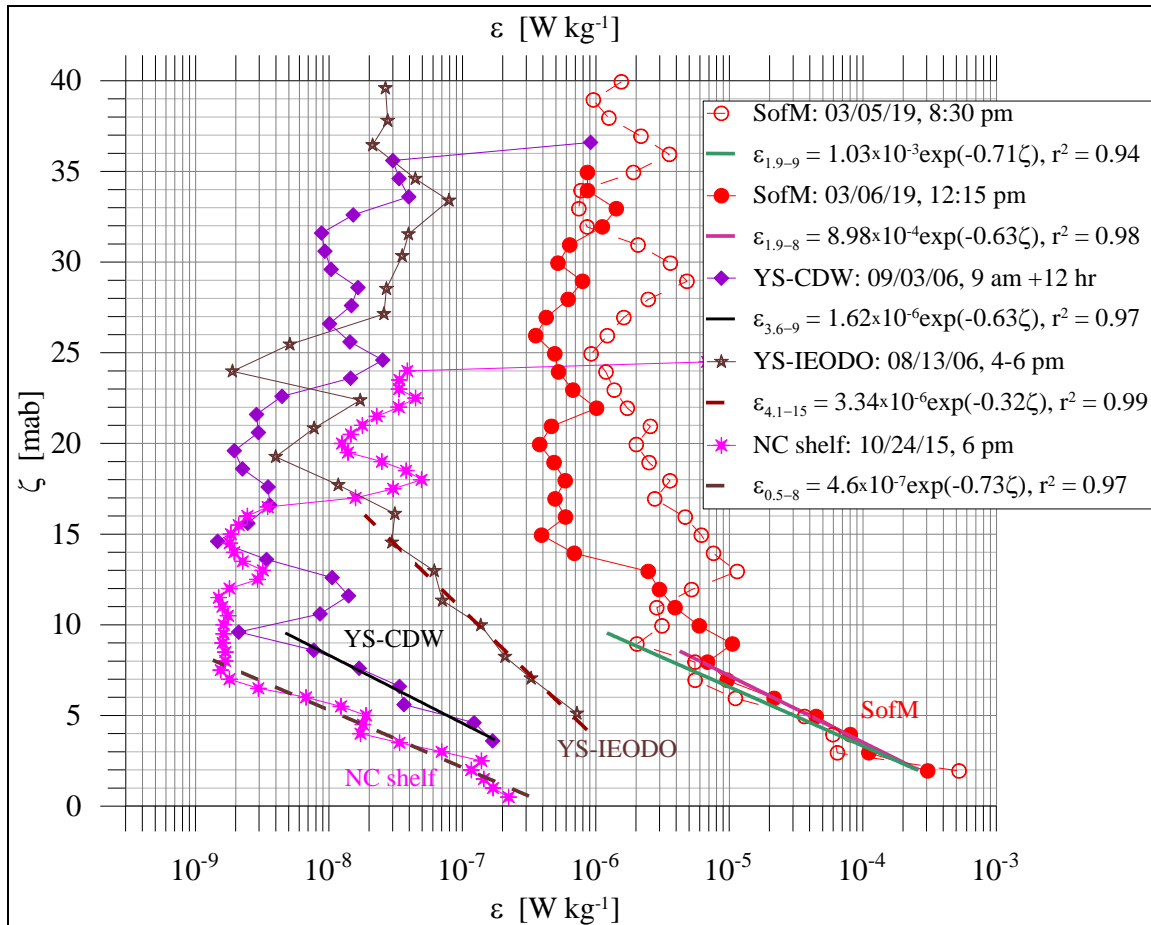
238 The BBL in well-mixed waters of MS was not distinct in thermohaline profiles due to  
 239 very small differences in temperature, salinity, and density near the bottom, but the BBL was  
 240 easy to define in the profiles of the squared mean shear  $Sh^2(\zeta)$  and the dissipation rate  $\varepsilon(\zeta)$ .  
 241 The TKE dissipation profiles  $\varepsilon(\zeta)$  shown in Figures 3 and 4 clearly indicate that starting from  
 242 some distance above the bottom  $\zeta_{BBL} = z_b - z_{BBL}$ , the dissipation rate sharply (exponentially)  
 243 increases toward the seafloor. All  $\varepsilon(\zeta)$  profiles in the MS showed an exponential dependence  
 244  $\varepsilon$  on  $\zeta$

$$245 \quad \varepsilon(\zeta) = \varepsilon_b e^{-\zeta/\Lambda} \quad (1)$$

246 where  $\varepsilon_b$  is the dissipation rate near the bottom and  $\Lambda$  a characteristic external length scale for  
 247 shear generated turbulence by mean (tidal) flow. Two additional  $\varepsilon(\zeta)$  profiles typical of March  
 248 5 and 6 are given in Figure 6 along with several profiles of  $\varepsilon(\zeta)$  obtained elsewhere in shallow  
 249 tidal seas, where an exponential decrease of  $\varepsilon$  with  $\zeta$  in BBL is demonstrated. These latter  
 250 data were collected in the Changjiang River Diluted Waters (YS-CDW) in the southwestern  
 251 Yellow Sea (Lozovatsky et al., 2012), in the IEODO region (YS-IEODO) in the southeastern  
 252 Yellow Sea (Lozovatsky et al., 2015) as well as on the North Carolina (NC) shelf (Lozovatsky et  
 253 al., 2017a). Note that an exponential decay of  $\varepsilon(\zeta)$  has been suggested by St. Laurent et al.  
 254 (2002) for deep-ocean BBL as a possible model of  $\varepsilon(\zeta)$  for turbulence generated by internal  
 255 tidal energy flux propagated upward over rough abyssal bathymetry.

256 All dissipation rate profiles in shallow BBL shown in Figure 6 can be well-approximated  
 257 by formulae (1) with coefficient of determination  $r^2 = 0.94 - 0.99$ . The tallest turbulent BBL with  
 258 exponentially varying  $\varepsilon(\zeta)$  was observed in the YS-IEODO region ( $\zeta_{BBL} \sim 15$  mab,  $\Lambda = 3.1$  m)  
 259 while a characteristic height of such BBL in other regions was  $\zeta_{BBL} \sim 8 - 9$  mab with  
 260  $\Lambda = 1.4 - 1.6$  m. It is worth noting that for all  $\varepsilon(\zeta)$  profiles in Figure 6, the external turbulent  
 261 scale  $\Lambda \sim 0.2\zeta_{BBL}$ , which is a typical value for boundary-induced turbulence (e.g., Monin &

262 Yaglom 1971). An exponential decrease of  $\varepsilon(\zeta)$  within the YS-IEODO BBL has been observed  
 263 by Lozovatsky et al. (2015) who argued that weak remnant stable stratification therein could  
 264 cause a faster decrease of  $\varepsilon$  with  $\zeta$  compared to an inverse-distance decay of  $\varepsilon(\zeta)$  that has  
 265 been discussed in numerous publications (e.g., Sanford & Lien 1999; Lozovatsky et al., 2008;  
 266 McMillan et al, 2016) in relation to marine BBL.



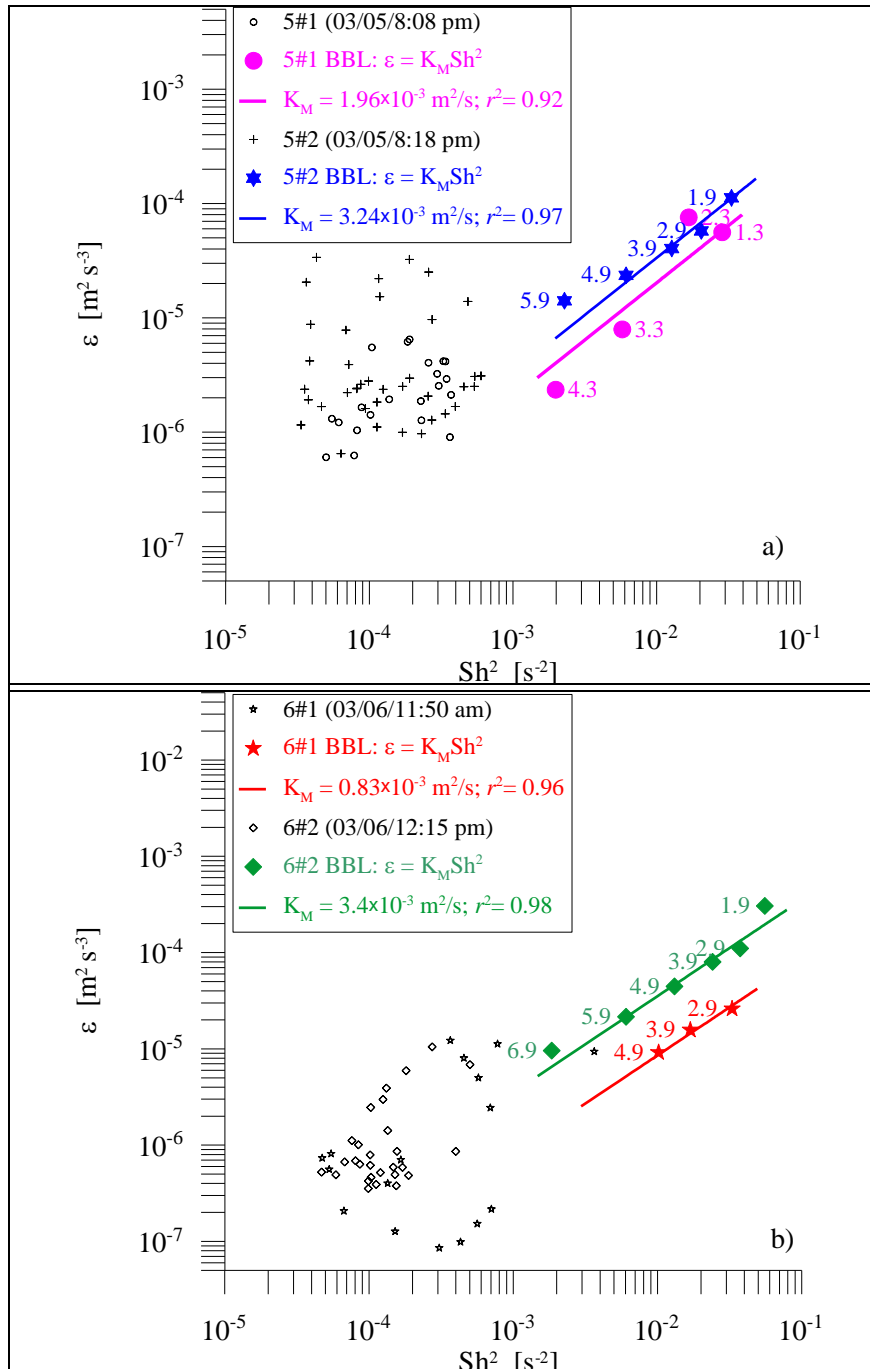
267  
 268 **Figure 6.** Examples of  $\varepsilon(\zeta)$  profiles showing an exponential increase of  $\varepsilon$  in the BBL toward the  
 269 seafloor at two stations in the Strait (March 5#3 and March 6#2, 2019) and typical  $\varepsilon(\zeta)$  profiles  
 270 measured in shallow tidal seas that exhibit exponential dependences  $\varepsilon(\zeta) \sim \varepsilon_b \exp(-\zeta/\Lambda)$  in BBL. Here,  
 271  $\varepsilon_b$  is a dissipation rate near the bottom and  $\Lambda$  a characteristic length-scale of BBL turbulence. Those  
 272 data have been reported by Lozovatsky et al. (2017a) for North Carolina shelf (NC shelf) and by  
 273 Lozovatsky et al (2012, 2015) for Changjiang River Diluted Waters (YS-CDW) in the southwestern  
 274 sector of Yellow Sea, and for the IEODO region (YS-IEODO) in the southeastern YS, respectively.  
 275 Parameters pertinent to the exponential approximations  $\varepsilon(\zeta)$  (straight lines) are in the legend.

276 While such an assumption for the MS BBL with very small  $N^2 \approx 10^{-7} - 10^{-6} \text{ s}^{-2}$  should be  
 277 considered with circumspection, Sakamoto & Akitomo (2006) argued that even weakly stable  
 278 stratification on the order of  $N^2 \approx 10^{-6} \text{ s}^{-2}$  may suppress BBL mixing specifically at high  
 279 latitudes. Rotation of tidal flow may also have a stabilizing effect on BBL turbulence, similar to  
 280 stable stratification and/or the Coriolis forces (e.g., Sakamoto & Akitomo 2008; Yoshikawa et al.  
 281 2010). Tidal ellipses in the SA region are so narrow (Figure 2b), however, that the flow  
 282 resembles a reversing rather than a rotating tide.

283 Thus, the exponential behavior of  $\varepsilon(\zeta)$  in the MS BBL as well as in several tidal  
 284 shallow seas could be considered to have different dynamics than log-layer boundary turbulence.  
 285 The clue is the exponential increase of mean squared shear in the BBL, which was presented as  
 286 an example for one of the stations in Figure 4. To verify the dependence between shear and  
 287 dissipation rate, we plotted  $\varepsilon$  vs.  $Sh^2$  for MS stations with  $z_b < 49 \text{ m}$ , where both VMP and  
 288 ADCP returned data close to the seafloor (1.3 – 2.9 mab). The data from “exponential BBLs” are  
 289 shown in Figure 7 by large symbols with adjacent numbers indicating the height from the  
 290 seafloor. If turbulence is solely generated by mean shear, for stationary turbulence the production  
 291  $K_M Sh^2$  term is balanced by viscous dissipation  $\varepsilon$  as

$$292 \quad K_M Sh^2 = \varepsilon, \quad (2)$$

293 where  $K_M$  is the eddy viscosity that parametrizes the vertical momentum flux  $\overline{u'w'} = -K_M Sh$ .  
 294 In Figure 7, the success of Eq.2 as an approximate empirical regression between  $\varepsilon$  and  $Sh^2$  in  
 295 the BBLs is apparent with high coefficients of determination  $r^2 = 0.92 - 0.98$ . The result signifies  
 296 that in the MS BBL (at  $\zeta > \sim 2 \text{ mab}$ ), the eddy viscosity  $K_M$  is independent of  $\zeta$  (constant  
 297 with height), varying in a relatively narrow range  $K_M = (0.83 - 3.4) \times 10^{-3} \text{ m}^2 \text{ s}^{-1}$ , though it  
 298 depends on the location in the Strait and the time of measurement (i.e., tidal phase); also see  
 299 Ross et al. (2019) who reported substantial tidal variability of  $K_M$  in a coastal plain estuary in  
 300 the French Atlantic Coast. Note that on March 5 and March 6, the VMP measurements were  
 301 taken in approximately the same transitional phase between low and high tide indicated in Figure  
 302 2.



303

304 **Figure 7.** The TKE dissipation rate  $\varepsilon$  vs. the squared vertical shear  $Sh^2$ : a) - stations 5#1 and 5#2, b) -  
 305 stations 6#1 and 6#2. Colored symbols belong to BBLs (see examples in Figures 4 and 6); the numbers  
 306 adjacent to the symbols specify the height above the bottom in mab. Parameters pertinent to the  
 307 approximations by Eq. 2 (eddy viscosity and  $r^2$ ) are in the legend.

308

309 The estimates of  $K_M$  allow assessing the possible thickness of the turbulent BBL  $h_{tbl}$  over  
 310 a bottom roughness. Yoshikawa et al. (2010) suggested that rotating tidal currents over a large  
 311 continental shelf affect the thickness of the Ekman BBL. Considering, however, that background  
 312 rotation associated with strong reversing tidal currents is negligible in such narrow channels as  
 313 SA, it is not possible to use the classical Ekman BBL height formulae in this case (Pedlosky  
 314 1987), but analogous to the Stokes oscillatory boundary layer (e.g., Krstic & Fernando, 2001),  
 315 thickness of the reversing tidal turbulent BBL  $h_{tbl}$  over rough bathymetry composed of hard  
 316 substratum (Simeoni et al., 1997) can be written as

$$317 \quad h_{tbl} = \left( \frac{2K_M}{\omega_{td}} \right)^{1/2}, \quad (3)$$

318 where  $\omega_{td} = 1.41 \times 10^{-4} \text{ s}^{-1}$  the semidiurnal tidal frequency. Using the estimates for the present  
 319 case  $K_M = (0.83 - 3.4) \times 10^{-3} \text{ m}^2\text{s}^{-1}$ ,  $h_{tbl}$  is found to be in the range 3.5 – 6.9 m. This is in general  
 320 agreement with data shown in Figure 7, where the height of the “exponential BBL” varies  
 321 between 4.3 and 6.9 mab. Thus, reversing tidal currents in a channel of the ilk of SA may create  
 322 a specific regime of strong ( $\varepsilon_b \sim 10^{-3} \text{ Wkg}^{-1}$ ) bottom-generated turbulence, which can be  
 323 characterized by a constant eddy viscosity and a TKE dissipation rate that exponentially decays  
 324 toward the water interior. The upper boundary of the exponential decay region of turbulence in  
 325 the northern MS is 4 - 7 mab for a transitional tidal phase, characterized by a characteristic tidal  
 326 velocity  $\sim 1 \text{ ms}^{-1}$  and eddy viscosity  $\sim 10^{-3} \text{ m}^2\text{s}^{-1}$ .

#### 327 **4 Summary**

328 First ever measurements of turbulence in the northeastern Strait of Magellan were taken  
 329 during March 2 – 6, 2019. A vertical microstructure profiler (VMP) and a shipboard acoustic  
 330 Doppler current profiler (ADCP) were used to obtain estimates of the TKE dissipation rate and  
 331 vertical shear at several stations (the bottom depth ranged between 25 and 55 m), respectively, in  
 332 the Segunda Angostura region to the north of Punta Arenas. During the field campaign, tidal  
 333 elevation varied in the range  $\pm \sim 1.5 \text{ m}$ . At the time of microstructure measurements, the speed  
 334 of reversing tidal currents was 0.8 - 1.2  $\text{ms}^{-1}$ . After a mild storm, entire water column became  
 335 well mixed with the median TKE dissipation rate above the bottom boundary layer  
 336  $\varepsilon_{med}^{MS} = 1.2 \times 10^{-6} \text{ Wkg}^{-1}$ , which was about an order of magnitude higher compared to the surface

337 mixed layer turbulence measured under moderate winds in typical ocean. This was associated  
338 with strong,  $(1-2) \times 10^{-2} \text{ s}^{-1}$ , vertical shear in the water interior that yielded gradient Richardson  
339 numbers  $Ri < 10^{-1} - 10^{-2}$ , which is well below the lower critical value threshold favorable for  
340 shear-induced turbulence. The dissipation rate near the seabed in MS was close to  $\varepsilon_b \approx 10^{-3}$   
341  $\text{Wkg}^{-1}$ . Note that Thomson et al. (2012) reported the tidally-induced near-bottom dissipation rate  
342 in the Puget Sound, WA, USA, which was as high as that measured in the Strait of Magellan,  
343 namely  $\varepsilon_b \sim 10^{-4} - 10^{-3} \text{ Wkg}^{-1}$ . During microstructure measurements, the tidal-current generated  
344 turbulent BBL height was  $\sim 4 - 7 \text{ m}$ , with an exponential decay of the dissipation rate and the  
345 vertical shear toward the water interior. In the exponentially varying regime, the eddy viscosity  
346 was found to be  $K_M = (0.83 - 3.4) \times 10^{-3} \text{ m}^2\text{s}^{-1}$ , independent of the vertical coordinate  $\zeta$  but  
347 dependent on tidal phase and location. Note that the eddy viscosity as high as  $10^{-2} - 10^{-1} \text{ m}^2\text{s}^{-1}$   
348 has been reported by Ross et al. (2019) for the spring tide in a plain estuary on the French  
349 Atlantic Coast. The results of the pilot field campaign described in this paper provided first yet  
350 limited information on the specifics of turbulence in the Magellan Strait, calling for further  
351 comprehensive investigations.

## 352 **Acknowledgements**

353 We are greatly thankful to the crew of the vessel Marypaz II for immense help during the VMP  
354 measurements. The research cruise was funded by the Marine Energy Research & Innovation  
355 Center of Chile (MERIC), CORFO project 14CEI2-28228. Chilean scientists were supported by  
356 MERIC and Research Internationalization Grant of the Pontificia Universidad Católica de Chile  
357 (grant no. PUC1566). The University of Notre Dame participants were partially supported  
358 through the 2018-2019 Luksic Family Collaboration Grant Award  
359 ([https://international.nd.edu/faculty-research/grants-and-funding/luksic-family-collaboration-](https://international.nd.edu/faculty-research/grants-and-funding/luksic-family-collaboration-grant/luksic-family-collaboration-grant-awardees/)  
360 [grant/luksic-family-collaboration-grant-awardees/](https://international.nd.edu/faculty-research/grants-and-funding/luksic-family-collaboration-grant/luksic-family-collaboration-grant-awardees/)). During the preparation of this paper, Notre  
361 Dame group was supported by ONR Grants N00014-17-1-3195 (dealing with air-sea interactions  
362 with EM ducting) as well as N00014-18-1-2472 (shelf/BBL turbulence with applications to  
363 marine fog genesis).

## 364 **Conflict of Interest**

365 The authors declare no conflicts of interest relevant to this study.

366 **Data Availability Statement**

367 The data used in this paper is available upon request from the corresponding author. Data  
368 management repository available at  
369 [https://drive.google.com/drive/folders/1mVA--r4dQ9qVBgSmxNQILcQJ\\_5ypC\\_93?usp=sharing](https://drive.google.com/drive/folders/1mVA--r4dQ9qVBgSmxNQILcQJ_5ypC_93?usp=sharing)

370  
371 **References**

- 372 Acevedo, J., Plana, J., Aguayo-Lobo, A., & Pastene, L. A. (2011). Surface feeding behavior of  
373 humpback whales in the Magellan Strait. *Revista de Biología Marina y Oceanografía*  
374 *46(3)*, 483-490. <http://dx.doi.org/10.4067/S0718-19572011000300018>
- 375 Brun, A.A., Ramirez, N., Pizarro, O., & Piola, A.R. (2020). The role of the Magellan Strait on  
376 the southwest South Atlantic shelf. *Estuarine, Coastal and Shelf Science* *237* (2020)  
377 106661, 1-11. <https://doi.org/10.1016/j.ecss.2020.106661>
- 378 Garreaud, R., Lopez, P., Minvielle, M., & Rojas, M. (2013). Large-scale control on the  
379 Patagonian climate. *Journal of Climate*, *26(1)*, 215-230.
- 380 Goodman, L., Levine, E.R., & Lueck, R.G. (2006). On measuring the terms of the turbulent  
381 kinetic energy budget from an AUV. *Journal of Atmospheric and Oceanic Technology*, *23*,  
382 977–990. <http://journals.ametsoc.org/doi/abs/10.1175/JTECH1889.1>
- 383 Guerra, M., & Thomson, J. (2017). Turbulence measurements from five-beam acoustic doppler  
384 current profilers. *Journal of Atmospheric and Oceanic Technology*, *34*, 1267–1284.  
385 <https://doi.org/10.1175/JTECH-D-16-0148.1>
- 386 Horwitz, R., & Hay, A. (2017). Turbulence dissipation rates from horizontal velocity profiles at  
387 mid-depth in fast tidal flows. *Renewable Energy*, *114*, 283–296,  
388 doi:10.1016/j.renene.2017.03.062
- 389 Jinadasa, S.U.P., Lozovatsky, I., Planella-Morató, J., Nash, J.D., MacKinnon, J.A., Lucas, A.J.,  
390 Wijesekera, H.W., & Fernando, H.J.S. (2016). Ocean turbulence and mixing around Sri  
391 Lanka and in adjacent waters of the northern Bay of Bengal. *Oceanography* *29*, 170–179.  
392 <http://dx.doi.org/10.5670/oceanog.2016.49>
- 393 Krstic, A., & Fernando, H.J.S. (2001). The nature of rough-wall oscillatory boundary layers. *J*  
394 *Hydraulic Research*, *39(6)*, 655-666. <https://doi.org/10.1080/00221686.2001.9628294>

395 Lozovatsky, I.D., Liu, Z., Hao, W., & Fernando, H.J.S. (2008). Tides and mixing in the  
396 northwestern East China Sea. Part II: The near-bottom turbulence. *Continental Shelf*  
397 *Research*, 28(2), 338-350. doi:10.1016/j.csr.2007.08.007

398 Lozovatsky, I., Liu, Z., Fernando, H.J.S., Armengol, J., & Roget, E. (2012). Shallow water tidal  
399 currents in close proximity to the seafloor and boundary-induced turbulence. *Ocean*  
400 *Dynamics*, 62, 177-201. doi:10.1007/s10236-011-0495-3.

401 Lozovatsky, I., Lee, J.-H., Fernando, H.J.S., Kang, S.K., & Jinadasa, S.U.P. (2015). Turbulence  
402 in the East China Sea: The summertime stratification. *Journal Geophysical Research:*  
403 *Oceans*, 120, 1856–1871. doi: 10.1002/2014JC010596

404 Lozovatsky, I., Planella-Morato, J., Shearman, K., Wang, Q., & Fernando, H.J.S. (2017a). Eddy  
405 diffusivity and elements of mesoscale dynamics over North Carolina shelf and contiguous  
406 Gulf Stream waters. *Ocean Dynamics* 67, 783-798. doi 10.1007/s10236-017-1059-y

407 Lozovatsky, I., Fernando, H.J.S., Planella-Morato, J., Liu, Z., Lee, J.-H., & Jinadasa, S.U.P.  
408 (2017b). Probability distribution of turbulent kinetic energy dissipation rate in ocean:  
409 Observations and approximations. *Journal Geophysical Research: Oceans* 122, 8293-  
410 8308. doi 10.1002/2017JC013076

411 Lozovatsky I., Pirro, A., Jarosz, E., Wijesekera, H.W., Jinadasa, S.U.P., & Fernando, H.J.S.  
412 (2019). Turbulence at the periphery of Sri Lanka dome. *Deep Sea Research II*, 168,  
413 104614:1-8. <https://doi.org/10.1016/j.dsr2.2019.07.002>

414 Lozovatsky, I., C. Wainwright, E. Creegan, and H. J. S. Fernando, 2021: Ocean turbulence and  
415 mixing near the shelf break southeast of Nova Scotia. *Boundary-Layer Meteor.* **181**, 425-  
416 441. <https://doi.org/10.1007/s10546-020-00576-z>

417 Lutz, V., Frouin, R., Negri, R., Silva, R., Pompeu, M., Rudorff, N., Cabral, A., Dogliotti, A., &  
418 Martinez, G. (2016). Bio-optical characteristics along the Straits of Magallanes.  
419 *Continental Shelf Research* 119, 56–67.

420 McMillan, J.M., Hay, A.E., Lueck, R.G., & Wolk, F. (2016). Rates of dissipation of turbulent  
421 kinetic energy in a high Reynolds number tidal channel. *Journal Physical Oceanography*,  
422 33, 817–837, doi:10.1175/JTECH-D-15-0167.1

423 McMillan, J.M., & Hay, A.E. (2017). Spectral and structure function estimates of turbulence  
424 dissipation rates in a high-flow tidal channel using broadband ADCPs. *Journal of*  
425 *Atmospheric and Oceanic Technology*, 34, 5–20, doi:10.1175/JTECH-D-16-0131.1.

426 Medeiros, Carmen & Bjorn Kjerfve. (1988). Tidal characteristics of the Strait of Magellan.  
427 *Continental Shelf Research*, 8(8), 947-960.

428 Monin, A.S., & Yaglom, A.M. (1971). Statistical Fluid Mechanics: Mechanics of Turbulence, 1.  
429 MIT Press, Cambridge, MA, 782pp.

430 Pedlosky, J. (1987). *Geophysical Fluid Dynamics*. 2d ed. Springer-Verlag, 710 pp.  
431 <https://doi.org/10.1007/978-1-4612-4650-3>

432 Ross, L., Huguenard, K., & Sottolichio, A. (2019).: Intratidal and fortnightly variability of  
433 vertical mixing in a macrotidal estuary: The Gironde. *Journal of Geophysical Research:*  
434 *Oceans*, 124, 2641–2659. <https://doi.org/10.1029/2018JC014456>

435 Roget, E., Lozovatsky, I., Sanchez, X., & Figueroa, M. (2006). Microstructure measurements in  
436 natural waters: Methodology and applications. *Progress in Oceanography* 70, 123-148.

437 Sakamoto, K., & Akitomo, K. 2006: Instabilities of the tidally induced bottom boundary layer in  
438 the rotating frame and their mixing effect. *Dynamics of Atmospheres and Oceans* 41, 191–  
439 211.

440 Sanford, T.S., and Lien, R.-C. (1999). Turbulent properties in a homogeneous tidal boundary  
441 layer. *Journal of Geophysical Research: Oceans* 104, (C1), 1245–1257.

442 Simeoni, U., Fontolan, G., & Colizza, E. (1997). Geomorphological characterization of the  
443 coastal and marine area between Primera and Segunda Angostura, Strait of Magellan  
444 (Chile) *Journal of Coastal Research*, 13, No.3, 916-924.

445 St. Laurent, L.C., Simmons, H.L., & Jayne, S.R. (2002). Estimating tidally driven mixing in the  
446 deep ocean, *Geophysical. Research Letters* 29(23), 2106, doi:10.1029/2002GL015633

447 Thomson, J., Polagye, B., Durgesh, V., & Richmond, M.C. (2012). Measurements of turbulence  
448 at two tidal energy sites in Puget Sound, WA, *IEEE Journal of oceanic engineering*, 37(3),  
449 363-374

450 Yoshikawa, Y., Endoh, T., Matsuno, T., Wagawa, T., Tsutsumi, E., Yoshimura, H., & Morii, Y.  
451 (2010). Turbulent bottom Ekman boundary layer measured over a continental shelf.  
452 *Geophysical. Research Letters* 37, L15605. doi: 10.1029/2010GL044156

453 Wolk, F. & Lueck, R. (2012). VMP turbulence profiler measurements in a tidal channel.  
454 *Rockland Technical Note 024*. 2012-06-30. [https://rocklandscientific.com/wp-](https://rocklandscientific.com/wp-content/uploads/2021/12/TN_024_VMP_in_Tidal_Channels.pdf)  
455 [content/uploads /2021/12/TN\\_024\\_VMP in Tidal Channels.pdf](https://rocklandscientific.com/wp-content/uploads/2021/12/TN_024_VMP_in_Tidal_Channels.pdf)

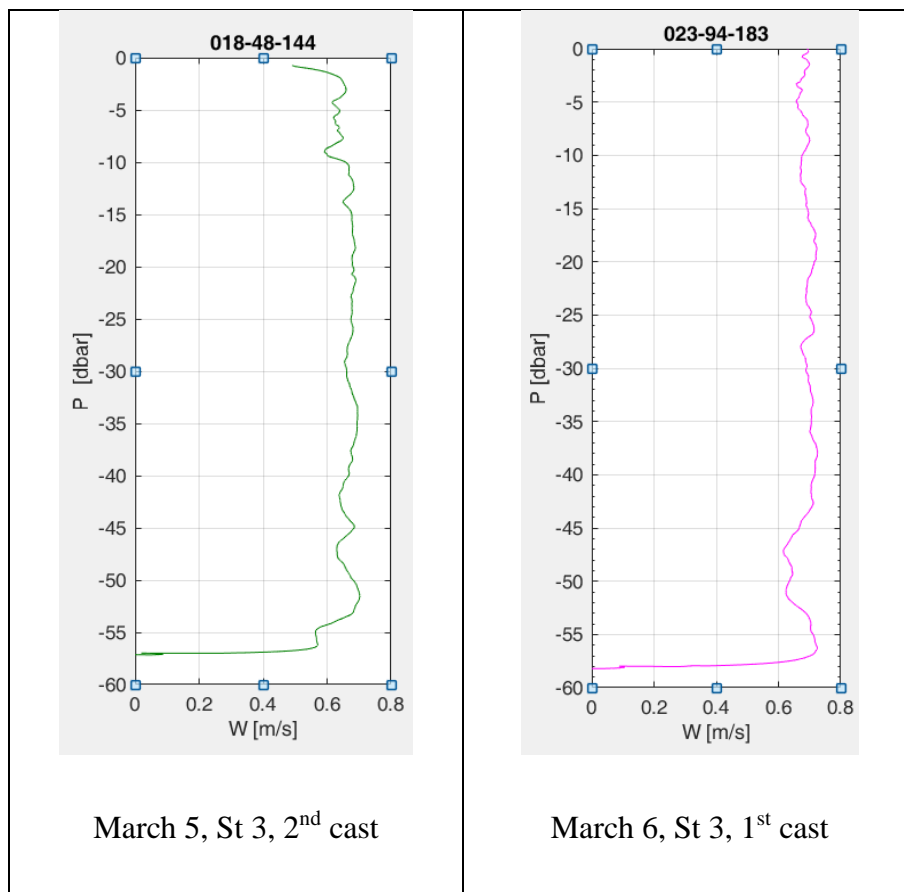
456

457

458 **Appendix**

459 Examples of the VMP sinking velocity profiles  $W(P)$  shown in Fig. A1 indicate fairly  
460 undisturbed almost constant  $W(P) \sim 0.7$  m/s during a major portion of the casts and a sharp drop of  
461  $W(P)$  to zero at the end of the casts ( $P$  is pressure).

462



463 **Figure A1.** The VMP sinking velocity profiles for two casts taken in the Magellan Strait on March 5 and  
464 6, 2019 (see stations in Figure 1).